CSIRO PUBLISHING

Australian Journal of Physics

Volume 50, 1997
© CSIRO Australia 1997

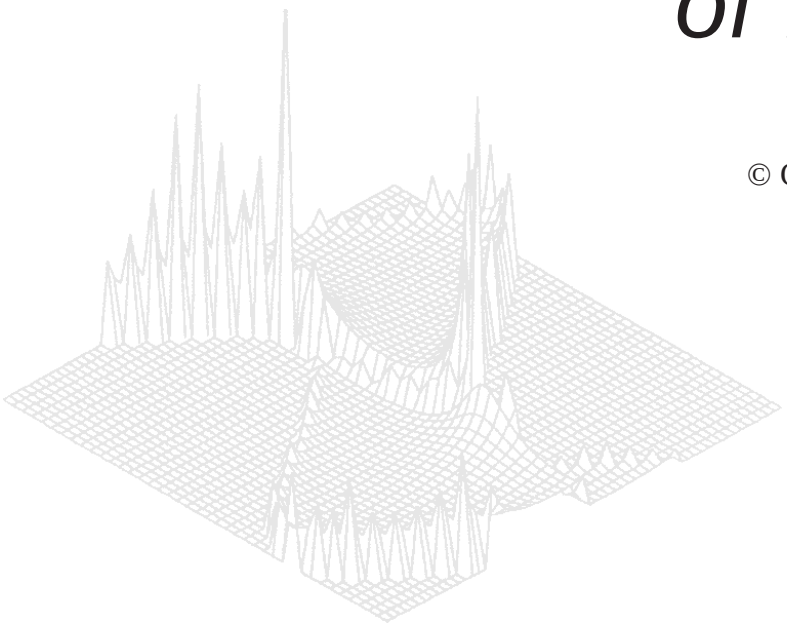

A journal for the publication of
original research in all branches of physics

www.publish.csiro.au/journals/ajp

All enquiries and manuscripts should be directed to
Australian Journal of Physics
CSIRO PUBLISHING
PO Box 1139 (150 Oxford St)
Collingwood Telephone: 61 3 9662 7626
Vic. 3066 Facsimile: 61 3 9662 7611
Australia Email: peter.robertson@publish.csiro.au

Published by **CSIRO** PUBLISHING
for CSIRO Australia and
the Australian Academy of Science

Aust. J. Phys., 1997, **50**, 975–1009

Aspects of Optical Properties in Conventional and Oxide Superconductors*

F. Marsiglio[A,B,C,D] *and J. P. Carbotte*[B,C]

[A] Neutron & Condensed Matter Science, AECL, Chalk River Laboratories, Chalk River, Ontario K0J 1J0, Canada.
[B] Department of Physics & Astronomy, McMaster University, Hamilton, Ontario L8S 4M1, Canada.
[C] Canadian Institute for Advanced Research, McMaster University, Hamilton, Ontario L8S 4M1, Canada.
[D] Present address: Department of Physics, University of Alberta, Edmonton, Alberta T6G 2J1, Canada.

Abstract

We review the effect of elastic and inelastic scattering on the normal state infrared conductivity, and describe modifications to the real and imaginary parts which result from a transition to an s-wave superconducting state. The zero frequency limit of the imaginary part is related to the temperature-dependent penetration depth and, at finite frequency, provides information about the superconducting gap. In the high T_c cuprates the gap appears to have d-wave symmetry. This profoundly modifies both the real and the imaginary parts of the optical conductivity. After describing these modifications we introduce the conductivity-derived scattering rate, which directly probes the inelastic scattering processes, and is much larger in the oxides than in conventional superconductors. This quantity is also significantly modified by the d-wave symmetry of the gap.

1. Introduction

In this paper we will review some of the properties of the optical conductivity of normal metals and superconductors. We begin with a brief discussion of the Drude model, which applies to free electrons in the normal state that undergo scattering off static impurities, with a constant (i.e. temperature and momentum independent) elastic scattering rate $1/\tau$. In the more realistic situation there will also be inelastic scattering processes, for example due to the electron interaction with lattice vibrations. At any finite temperature lattice vibrations (phonons) will be thermally excited and, like impurities, can scatter electrons. However, such processes are dependent on the thermal phonon population, which is strongly temperature dependent. This leads to an effective Drude width $1/\tau(T)$, which decreases rapidly as the temperature is lowered and approaches zero as $T \to 0$. In addition phonon-assisted absorption is possible, whereby the incoming photon energy and momentum are taken up by an excited electron plus phonon. Such phonon-assisted processes arise even at zero temperature, albeit with a threshold energy required equal to the minimum phonon energy. Since the phonon density

* Refereed paper based on a contribution to the Fifth Gordon Godfrey Workshop on Superconductivity held at the University of New South Wales, Sydney, in November 1995.

© CSIRO Australia 1997 10.1071/PH97005 0004-9506/97/060975$15.00

of states varies as ω^2 in the Debye regime this absorption onset will be gradual, and will extend over the entire phonon energy scale. Thus at low temperature there will be two distinct regions. The first will be a low energy rapidly narrowing Drude contribution, and the second will be a relatively temperature-independent phonon-assisted region, extending over the phonon energy domain; there will be little overlap of the two regions if the inelastic scattering rate is not very strong. As the electron–phonon spectral density increases in strength the overlap also increases. Too strong an impurity scattering rate can also blur the distinction between the two regions.

Next we consider the modifications introduced when a transition to a superconducting state occurs. For an isotropic s-wave superconductor the real (absorptive) part of the conductivity becomes gapped up to twice the value of the single-particle gap Δ at $T = 0$. The missing spectral weight is transferred to the superfluid, which produces a delta function contribution at zero frequency. At finite temperature some normal fluid remains and some absorption in the form of a Drude-like peak of reduced weight and width is also present. Nonetheless, the finite temperature gap value remains clearly visible in the conductivity. The product of the frequency times the imaginary part of the conductivity also carries information about the gap and shows a clear cusp-like structure at a frequency equal to 2Δ for finite values of $1/\tau$ in the BCS limit. This structure is gradually smeared and slightly shifted in frequency as $1/\tau$ increases. The cusp remains clearly visible even at finite temperature.

When inelastic scattering is included the BCS results become modified. In the special case of $1/\tau = 0$ (i.e. the clean limit) neither the real nor the imaginary part of the conductivity shows a clear onset at 2Δ, although both are affected by the superconducting transition. When impurities are introduced, however, a sharp absorption edge and a cusp are restored to the real and imaginary parts of the conductivity, respectively.

In the case of d-wave superconductivity the situation is very different. The single-particle excitation spectrum has nodes at the Fermi surface, so the conductivity tends to resemble that of the normal state. There is no clear characteristic absorption edge that can be associated with the growth of a superconducting order parameter. Similar remarks apply to the conductivity-derived frequency-dependent scattering rate $1/\tau(\nu)$, to be defined in the next section. The low frequency part of this rate provides a signature of the gap symmetry, with qualitatively different behaviour for s- and d-wave symmetry. The high frequency part reflects inelastic scattering processes, and so may provide information about the superconducting mechanism.

2. Normal State Conductivity

The complex Drude conductivity $\sigma(\nu)$ is given as a function of frequency ν by the well-known expression (Ashcroft and Mermin 1976)

$$\sigma(\nu) = \frac{ne^2}{m} \frac{1}{1/\tau - i\nu}\,, \tag{1}$$

where n, e, and m are the free electron density, charge magnitude, and mass, respectively, and τ $(1/\tau)$ is an electron relaxation time (scattering rate). The

relaxation time can come from a variety of sources; the simplest is ordinary elastic impurity scattering. The scattering rate $1/\tau$ is then independent of temperature, and here we assume it is independent of momentum. Note that there are two simple ways (Dolgov *et al.* 1991; Shulga *et al.* 1991) to infer the scattering rate from equation (1),

$$1/\tau = \frac{ne^2}{m} Re\left(\frac{1}{\sigma(\nu)}\right), \tag{2}$$

which requires independent knowledge of the prefactor ne^2/m, and

$$1/\tau = \nu\sigma_1(\nu)/\sigma_2(\nu), \tag{3}$$

where $\sigma_1(\nu)$ and $\sigma_2(\nu)$ denote the real and imaginary parts of the conductivity. This latter means has the obvious advantage of not requiring independent knowledge of the plasma frequency ω_P, where $\omega_P^2 \equiv 4\pi ne^2/m$. The function $\sigma_1(\nu)$ ($\sigma_2(\nu)$) has a maximum (minimum) at $\nu = 0$. They both have widths at half-maximum equal to $1/\tau$. Sketches are provided later (in Figs 6–9). In the asymptotic limit ($\nu \to \infty$) $\sigma_1(\nu)$ approaches zero as $1/\nu^2$ and $\nu\sigma_2(\nu)$ approaches the constant ne^2/m. In the clean limit there is very little impurity scattering and $1/\tau$ approaches zero. This implies a narrow Drude form for $\sigma_1(\nu)$ and $\sigma_2(\nu)$. Conversely in the dirty limit ($1/\tau \to \infty$) the Drude form becomes broad. One can easily see from (1) that mathematically in the clean limit $\sigma_1(\nu)$ approaches a delta-function at the origin, indicating that at zero frequency the clean metal (i.e. without impurities) is a perfect conductor while at finite frequency it is a perfect reflector (no absorption).

Equations (2) and (3) apply to the Drude model. However, following Dolgov *et al.* (1991) and Shulga *et al.* (1991), we generalise these definitions to include inelastic scattering processes, thereby defining $1/\tau(\nu)$ (equation 2) and $1/\tau^*(\nu)$ (equation 3), respectively. As we shall see later in this review, $1/\tau(\nu)$ in particular can be used to extract meaningful characteristics in the superconducting state as well.

We have mentioned the plasma frequency ω_P. One means of extracting this quantity is the conductivity sum rule (Kubo 1957),

$$\int_0^\infty \sigma_1(\nu)d\nu = \frac{\omega_P^2}{8\pi}, \tag{4}$$

which requires a measurement of the real part of the conductivity over all frequencies. In practice one is often interested in the electronic properties of a particular band near the Fermi surface. One should then terminate the frequency sum before the region involving interband transitions is reached. Then, of course, the free electron density in the definition of the plasma frequency corresponds to the electron density associated with this particular band.

As an aside we should add some remarks concerning the measurement of the complex conductivity. A common method is to measure the reflectance (Timusk and Tanner 1989; Tanner and Timursk 1992) as a function of frequency, usually at normal incidence. Possible alternatives are transmission measurements, which

can be used for thin films, and absorption measurements which can be performed using bolometry. Here we focus on the reflectance $R(\nu)$, which is defined as the absolute ratio squared of reflected over incident electromagnetic wave amplitude (Ziman 1972). The complex reflectivity is defined as

$$r(\nu) \equiv R^{\frac{1}{2}}(\nu) \exp\left(i\theta(\nu)\right), \tag{5}$$

where $\theta(\nu)$ is the phase, and is obtained through a Kramers–Kronig relation (Timusk and Tanner 1989; Tanner and Timusk 1992)

$$\theta(\nu) = \frac{\nu}{\pi} \int_0^\infty \frac{\ln R(\nu') - \ln R(\nu)}{\nu^2 - \nu'^2} d\nu' . \tag{6}$$

The reflectivity is related to the complex index of refraction $N(\nu)$:

$$r(\nu) \equiv \frac{N(\nu) - 1}{N(\nu) + 1}, \tag{7}$$

which in turn is simply related to the dielectric function $\epsilon(\nu)$, or complex conductivity $\sigma(\nu)$:

$$\epsilon(\nu) \equiv N^2(\nu) = \epsilon_\infty + \frac{4\pi i \sigma(\nu)}{\nu} . \tag{8}$$

Here ϵ_∞ in principle approaches unity at infinite frequency; in practice it takes on some value greater than unity beyond the intraband frequency regime, and this value is used in (8). We note that the Kramers–Kronig relation requires knowledge of the reflectance for all frequencies. In practice extrapolation functions (Hagen–Rubens form at low frequency and some power law decay at high frequency) are utilised to complete the integral. While these procedures introduce some uncertainty into the 'measured' conductivity, for the purpose of this review we view the real and imaginary parts of the conductivity (which follow on *an equal footing* from equation (8)) as the 'raw data'. For completeness we illustrate in Fig. 1 the reflectance one expects to measure as a function of frequency for a hypothetical metal which has a Drude conductivity give by (1). Note the Hagen–Rubens form $R(\nu) \approx 1 - \sqrt{\frac{8}{\omega_P \tau} \frac{\nu}{\omega_P}}$ at lower frequency, and the relatively constant regime followed by a sharp plasma edge for the cases where $1/\tau \ll \omega_P$.

At finite temperature other imperfections arise: thermal fluctuations displace an ion of an otherwise perfect lattice off its equilibrium position. An electron can scatter off this imperfection as in the case of an impurity, except that now the scattering is inelastic, and the energy of the scattered electron changes. Overall energy is conserved, with the remaining energy difference taken up by the phonons. The number of thermally excited phonons is strongly dependent on temperature, so that the phonon-induced electron scattering rate is strongly temperature dependent, and vanishes as $T \to 0$. The degree of scattering will clearly depend on the density of phonon states, usually denoted $F(\omega)$. More precisely the electron

scattering from these states will be weighted by an electron–phonon matrix element, so that the relevant function is a weighted density of states sometimes called the electron–phonon spectral density $\alpha^2F(\omega)$ (also called the Eliashberg function in the Soviet literature). A more explicit form will be provided later.

One of the recurring themes of this paper is that there are many ways of characterising the electron scattering rate. We have already mentioned one in the context of impurity scattering, which is to use the electron transport properties, in this case the optical conductivity. A second means is through the single-particle propagator, whose pole acquires a finite imaginary part. This demonstrates that an electron can decay, i.e. scatter into another state. As will be discussed in the following paper (Marsiglio and Carbotte 1997, present issue p. 1011), the imaginary part of the electron self-energy gives the electron (i.e. quasiparticle) inverse lifetime (see, for example, Grimvall 1981; Allen and Mitrović 1982):

$$\Gamma(\omega,T) \equiv -2Im\Sigma(\omega,T)\,. \tag{9}$$

For example, the inverse quasiparticle lifetime, $\Gamma_{\mathrm{e-i}}$ for impurity scattering is simply

$$\Gamma_{\mathrm{e-i}} = 1/\tau\,, \tag{10}$$

which is identical to that inferred from the conductivity (Mahan 1981, 1987)*. For electron–phonon scattering, the result at the Fermi surface ($\omega = 0$) is (Grimvall 1981; Allen and Mitrović 1982)

$$\Gamma_{\mathrm{e-ph}}(T) = \frac{4\pi}{1+\lambda^*(T)} \int_0^\infty \alpha^2F(\omega)\mathrm{csch}(\beta\omega)d\omega\,, \tag{11}$$

where $\beta \equiv 1/k_BT$ is the inverse temperature. Here $\hbar$ has been set to unity, as is the Boltzmann constant k_B. The mass enhancement parameter $\lambda^*(T)$ is fully described later. To infer the low temperature behaviour of the quasiparticle lifetime (due to phonon scattering) we adopt a Debye model, applicable to most metals for sufficiently low frequency, so that $\alpha^2F(\omega) \propto \omega^2$ and

$$\Gamma_{\mathrm{Debye}}(T) \propto T^3\,. \tag{12}$$

Equation (12) is applicable only at the Fermi surface, as are the following expressions for the inverse lifetime. In the marginal Fermi liquid (MFL) model (Varma *et al.* 1989, 1990; Nicol *et al.* 1991) with coupling to charge and spin fluctuations the effective spectral density $\alpha^2F(\omega)$ is approximated by the functional form

$$\alpha^2F(\omega) \approx \tanh(\beta\omega/2)\,, \tag{13}$$

* Strictly speaking we should distinguish between τ and τ_{tr}, the latter being the transport-related scattering time, while the former is defined to mean a general scattering time, unweighted by the direction of scattering. However, for s-wave electron-impurity scattering, the two are equal. Similarly, there is a distinction between the electron–phonon spectral function $\alpha^2F(\omega)$, and $\alpha^2_{tr}F(\omega)$, which is used for transport properties. These two functions are often very similar, and for present purposes, the distinction will be ignored.

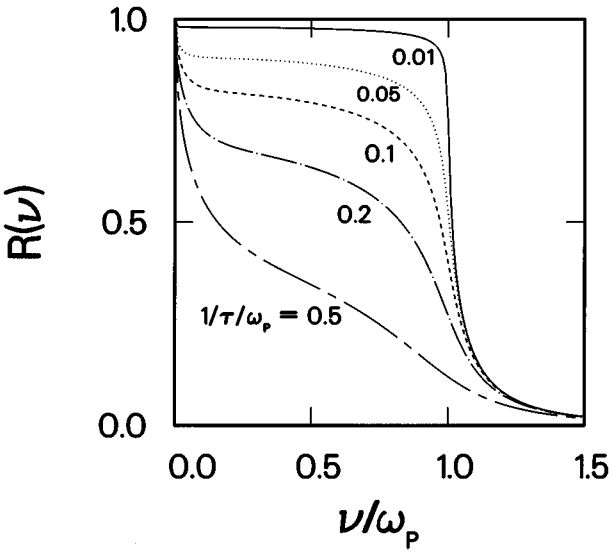

Fig. 1. Drude reflectance as a function of frequency normalised to the plasma frequency, for various values of the elastic scattering rate $1/\tau$. Note that the well-defined plasma edge occurs for $1/\tau \ll \omega_P$.

so that

$$\Gamma_{\rm MFL}(T) \propto T\,. \tag{14}$$

Such a temperature dependence is characteristic of various transport properties in the cuprate materials in the normal state, and has led in part to the popularity of the MFL model. In the nearly antiferromagnetic Fermi liquid model (NAFLM) (Millis *et al.* 1990; Monthoux and Pines 1993) electron scattering occurs by exchange of antiferromagnetic spin fluctuations. At low frequency the spin fluctuation spectral function is linear, $\alpha^2F(\omega) \approx \omega$, so that the inverse quasiparticle lifetime is

$$\Gamma_{\rm NAFLM}(T) \propto T^2\,. \tag{15}$$

These examples illustrate that the quasiparticle inverse lifetime can acquire very different temperature dependences, depending on the model boson which is the source of inelastic scattering. The key signature that a boson interacts strongly with electrons is a broad Drude width at high temperature which narrows considerably as the temperature is lowered to zero temperature.

The lack of scattering mechanisms makes absorption of incoming photons impossible, since momentum and energy conservation laws cannot be fulfilled simultaneously. With impurity scattering electrons can be promoted from below the Fermi surface to above with the required change in momentum taken up by the impurity site. The presence of inelastic scattering allows an electron to make a transition from below the Fermi surface to above through the creation of a phonon which takes up both the momentum and energy imbalance. Such a process is referred to as a Holstein or phonon-assisted absorption process. More

generally we refer to such a process as boson-assisted absorption. This absorption occurs even at zero temperature at frequencies beyond the minimum phonon energy (Ron 1963).

The derivation of the optical conductivity for a metal with these various scattering processes is given in several texts and reviews (Mahan 1981, 1987). Two routes can be followed, one based on a Boltzmann equation and the other based on the Kubo formula. We refer the reader to the references for such a derivation, and simply quote the final result, valid for an s-wave superconductor (Nam 1967; Lee *et al.* 1989; Bickers *et al.* 1990; Marsiglio *et al.* 1992) (in Marsiglio *et al.* the derivation for the phonon self-energy at $q = 0$ applies to the optical conductivity)

$$\sigma(\nu) = \frac{i}{\nu}\left(\Pi(\nu + i\delta) + \frac{ne^2}{m}\right), \tag{16}$$

where $\Pi(\nu + i\delta)$ is the paramagnetic response function given by

$$\Pi(\nu + i\delta) = \frac{ne^2}{m}\Bigg\{ -1 + \int_0^\infty d\omega \tanh(\beta\omega/2)\big(h_1(\omega, \omega+\nu) - h_2(\omega, \omega+\nu)\big) + \int_{-\nu}^{D} d\omega \tanh(\beta(\omega+\nu)/2)\big(h_1^*(\omega, \omega+\nu) + h_2(\omega, \omega+\nu)\big)\Bigg\}, \tag{17}$$

with

$$h_1(\omega_1, \omega_2) = \frac{1 - N(\omega_1)N(\omega_2) - P(\omega_1)P(\omega_2)}{2(\epsilon(\omega_1) + \epsilon(\omega_2))},$$

$$h_2(\omega_1, \omega_2) = \frac{1 + N^*(\omega_1)N(\omega_2) + P^*(\omega_1)P(\omega_2)}{2(\epsilon(\omega_2) - \epsilon^*(\omega_1))},$$

$$N(\omega) = \frac{\tilde{\omega}(\omega + i\delta)}{\epsilon(\omega + i\delta)} \qquad P(\omega) = \frac{\phi(\omega + i\delta)}{\epsilon(\omega + i\delta)},$$

$$\epsilon(\omega) = \sqrt{\tilde{\omega}^2(\omega + i\delta) - \phi^2(\omega + i\delta)}, \tag{18}$$

where D is a large cutoff to be taken to infinity for large electronic bandwidth.

These equations require knowledge of the pairing and renormalisation functions $\phi(\omega)$ and $\tilde{\omega}(\omega)$, respectively. In the superconducting state these are determined by solving the Eliashberg (1960) equations, which are provided for convenience in the following paper. For the moment we proceed with the normal state, so that $\phi(\omega) = 0$. Then

$$\text{Re } \tilde{\omega}_n(\omega + i\delta) = \omega - \int_0^\infty d\nu \alpha^2 F(\nu) \text{Re } \left[\psi\left(\tfrac{1}{2} + i\frac{\nu - \omega}{2\pi T}\right) - \psi\left(\tfrac{1}{2} - i\frac{\nu + \omega}{2\pi T}\right)\right], \tag{19}$$

$$\text{Im } \tilde{\omega}_n(\omega + i\delta) = \pi \int_0^\infty d\nu \alpha^2 F(\nu) \text{Re } \left[2N(\nu) + f(\nu + \omega) + f(\nu - \omega)\right] + \frac{1}{2\tau}, \tag{20}$$

where the subscript 'n' denotes normal state, $\psi(x)$ denotes the digamma function and $N(\nu)$ and $f(\omega)$ are the Bose and Fermi functions respectively. Note that the renormalisation function is simply related to the electron self-energy discussed earlier:

$$\tilde{\omega}_n(\omega + i\delta) \equiv \omega - \Sigma(\omega)\,. \tag{21}$$

We have also included the contribution from impurity scattering, in the Born approximation, which gives the last factor in (20). As is clear from these equations, the electron–phonon spectral function $\alpha^2F(\omega)$ determines the renormalisation due to the electron–phonon interaction given by the Hamiltonian

$$H_{\mathrm{e-ph}} = \sum_{\substack{\mathbf{k},\mathbf{k}'\\ \sigma\lambda}} g_{\mathbf{k},\mathbf{k}';\lambda} c^\dagger_{\mathbf{k}\sigma} c_{\mathbf{k}'\sigma} \left[a_{\mathbf{k}-\mathbf{k}';\lambda} + a^\dagger_{-\mathbf{k}+\mathbf{k}';\lambda}\right], \tag{22}$$

in which $g_{\mathbf{k},\mathbf{k}';\lambda}$ is the coupling for electron scattering from wave vector $\mathbf{k}'$ to $\mathbf{k}$ through the emission ($a^\dagger$) or absorption (a) of a phonon. The electron spin is σ, the phonon branch index is λ, and the phonon momentum is $\pm(\mathbf{k}-\mathbf{k}')$. In terms of $g_{\mathbf{k},\mathbf{k}';\lambda}$ the electron–phonon spectral function has the form

$$\alpha^2F(\nu) = \frac{\sum_{\mathbf{k}\mathbf{k}'} |g_{\mathbf{k},\mathbf{k}';\lambda}|^2 \delta\big(\nu - \omega_\lambda(\mathbf{k}-\mathbf{k}')\big)\delta(\epsilon_{\mathbf{k}})\delta(\epsilon_{\mathbf{k}'})}{\sum_{\mathbf{k}}\delta(\epsilon_{\mathbf{k}})}\,, \tag{23}$$

where $N(0) \equiv \sum_{\mathbf{k}} \delta(\epsilon_{\mathbf{k}})$ is the density of electron states at the Fermi surface. In fact, (23) gives a momentum independent function because the electron wave vectors have been averaged over the Fermi surface. Further justification of this procedure for most metals is found in Allen and Mitrović (1982).

In much of this review we will focus on measurements taken on the cubic perovskite $Ba_{1-x}K_xBiO_3$, which has a superconducting critical temperature $T_c = 29$ K. To model this material we will utilise an electron–phonon spectral function based on the generalised density of phonon states $G(\omega)$ obtained from neutron scattering (Loong *et al.* 1989, 1991), and scale the spectrum to yield a mass renormalisation parameter λ equal to unity. The more desirable procedure of using tunneling to extract $\alpha^2F(\omega)$ (McMillan and Rowell 1969) has some difficulties (Huang *et al.* 1990; Zasadzinski *et al.* 1991; Sharifi *et al.* 1991). The mass renormalisation parameter is given by

$$\lambda = 2\int_0^\infty \frac{\alpha^2F(\omega)}{\omega} d\omega \tag{24}$$

and also corresponds to the zero temperature limit of $\lambda^*(T)$ introduced earlier. We then parametrise the Coulomb repulsion through a structureless pseudopotential μ^*, as is usual. A value close to zero ($\mu^* = 0{\cdot}018$) is required to give $T_c = 29$ K. We show a plot of this model $\alpha^2F(\omega)$ in Fig. 2. The important thing to note is the maximum phonon energy scale, 70 meV. [Regarding units, they are used interchangeably in the literature, with the convention $1\ \mathrm{meV} = 11{\cdot}605\ \mathrm{K} = 8{\cdot}1\ \mathrm{cm}^{-1}$. Also, conductivity will sometimes be computed to be in meV (cm^{-1} or s^{-1}). These numbers are to be divided by $0{\cdot}592$ ($4{\cdot}77$ or $9{\times}10^{11}$), respectively to convert to practical units, $(\mathrm{ohm\ cm})^{-1}$.]

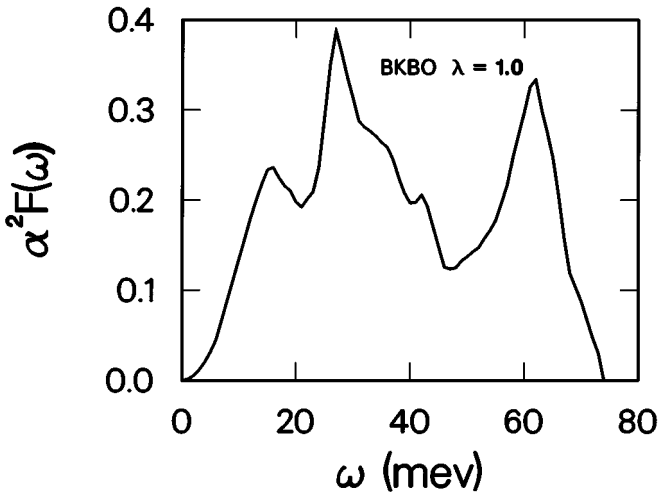

Fig. 2. Electron–phonon spectral function for BKBO, as determined by scaling the density of phonon states measured by Loong *et al.* (1991) using neutron scattering techniques.

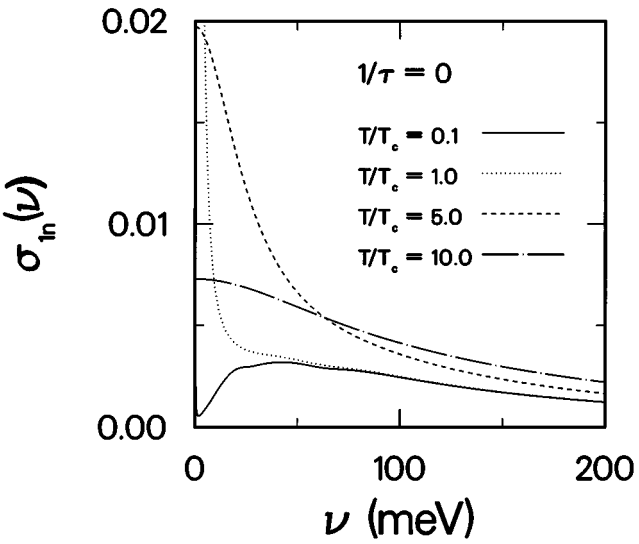

Fig. 3. Real part of the normal state conductivity (in units of ne^2/m) versus frequency in the clean limit ($1/\tau = 0$), plotted for various temperatures. Here $T_c = 29$ K. Because we are in the clean limit the conductivity is entirely due to phonon-assisted absorption. However, at any non-zero temperature, a Drude-like component is present.

Using this model for $\alpha^2F(\omega)$ we show the real part of the conductivity in the normal state in Fig. 3 for various temperatures referenced to the critical temperature (Marsiglio and Carbotte 1995) (hereafter we show conductivity in units of ne^2/m). We have included only the electron–phonon scattering and so refer to such cases as the clean limit ($1/\tau = 0$). Note that at essentially any nonzero temperature a Drude-like peak centred at the origin exists. At the highest temperature shown ($T/T_c = 10$, long dash-dotted curve) the Drude peak

is very broad, which occurs because of the large inelastic scattering rate as given by (11). In contrast, at the lowest temperature shown, a very narrow Drude peak is barely visible near the origin. At $T = 0$ no peak would be present, and all that would remain is the phonon-assisted conductivity at higher frequencies. Thus at any finite temperature, thermally populated phonons behave much like normal impurities as far as the optical conductivity is concerned.

This correspondence can be quantitatively demonstrated. By performing low frequency expansions we have previously shown (Marsiglio and Carbotte 1995) that the low frequency conductivity can be written in a Drude-like form

$$\sigma_{1\mathrm{Drude}} = \frac{ne^2}{m}\frac{1}{1+\tilde{\lambda}}\left(\frac{1/\tilde{\tau}}{\nu^2+(1/\tilde{\tau})^2}\right), \tag{25}$$

where $\tilde{\lambda}$ and $\tilde{\tau}$ are given by the expressions

$$1/\tilde{\tau}^2 \equiv \frac{\displaystyle\int_0^\infty \frac{\beta d\omega}{2}\mathrm{sech}^{\,2}(\frac{\beta\omega}{2})\frac{\tau^*(\omega)}{1+\lambda^*(\omega)}}{\displaystyle\int_0^\infty \frac{\beta d\omega}{2}\mathrm{sech}^{\,2}(\frac{\beta\omega}{2})\frac{\tau^*(\omega)^3}{1+\lambda^*(\omega)}}, \tag{26}$$

$$\frac{1}{1+\tilde{\lambda}} \equiv \frac{1}{\tilde{\tau}}\int_0^\infty \frac{\beta d\omega}{2}\mathrm{sech}^{\,2}\frac{\beta\omega}{2}\frac{\tau^*(\omega)}{1+\lambda^*(\omega)}. \tag{27}$$

In these definitions we have used the quantities

$$1/\tau^*(\omega) \equiv \frac{1/\tau + 2\mathrm{Im}\ \tilde{\omega}_n(\omega+i\delta)}{1+\lambda^*(\omega)}, \qquad 1+\lambda^*(\omega) \equiv \frac{\partial \mathrm{Re}\ \tilde{\omega}_n(\omega+i\delta)}{\partial\omega}. \tag{28}$$

These expressions apply for the normal state, with both electron-impurity and electron–phonon scattering included. They have been derived without fitting parameters. To examine how well they characterise the low frequency conductivity, we show results in Fig. 4 for various temperatures and impurity scattering rates. It is clear that over some frequency range (which increases as the temperature increases) the approximate results from equation (25) shown as dotted curves agree very accurately with the full results from (16), shown as solid curves. To further understand the significance of the Drude parameters, we note that the conductivity sum rule, applied to (25), gives

$$\int_0^\infty d\nu\sigma_{1\mathrm{Drude}}(\nu) = \frac{\pi}{2}\frac{ne^2}{m}\frac{1}{1+\tilde{\lambda}(T)}. \tag{29}$$

Note that $\tilde{\lambda}$ reduces to the mass renormalisation parameter λ (equation 24) as $T \to 0$. The missing area in (29) is accounted for by the boson-assisted contribution not included in (25), and is proportional to $\tilde{\lambda}$. Thus, to estimate the electron–phonon coupling strength one would measure the low frequency part of the conductivity, and evaluate the area under the Drude fit to determine the partial contribution given by (29). To obtain $\tilde{\lambda}$ one requires an independent

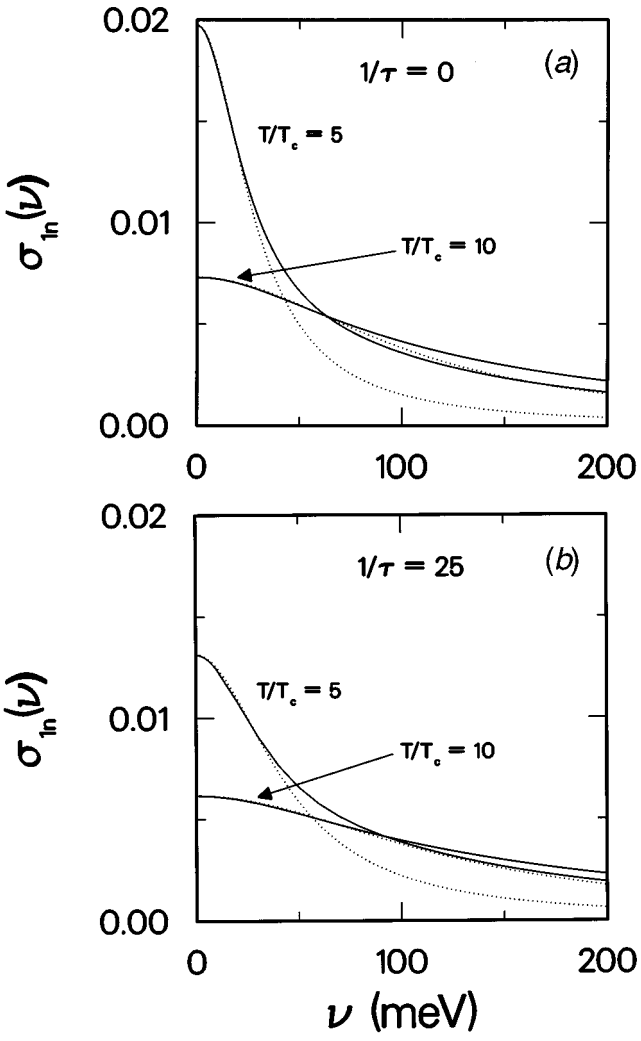

Fig. 4. A plot of $\sigma_{1n}(\nu)$ versus ν for (a) $1/\tau = 0$ and (b) $1/\tau = 25$ meV. The solid curves are the full numerical results, while the dotted curves are given by the Drude fit, equation (25). These are accurate at low frequency for all temperatures and impurity scattering rates.

estimate for the bare plasma frequency, say from penetration depth measurements (Basov *et al.* 1995). A more self-contained procedure is to measure the area at various temperatures, and in particular at high temperature. At very high temperature the electrons are essentially 'undressed' from the phonons, so $\tilde{\lambda}$ approaches zero. The area will then approach the value $\frac{\pi}{2}\frac{ne^2}{m}$. In Fig. 5$a$ we plot the Drude area normalised to this value as a function of temperature for various values of the impurity scattering rate $1/\tau$. Also shown on the same plot is the value of $\tilde{\lambda}(T)$ for the same impurity scattering rates. These latter curves fall to zero as T increases, while the area approaches unity due to the normalisation discussed above. As already mentioned the electron–phonon 'undressing' at high temperatures occurs because the phonons appear as static,

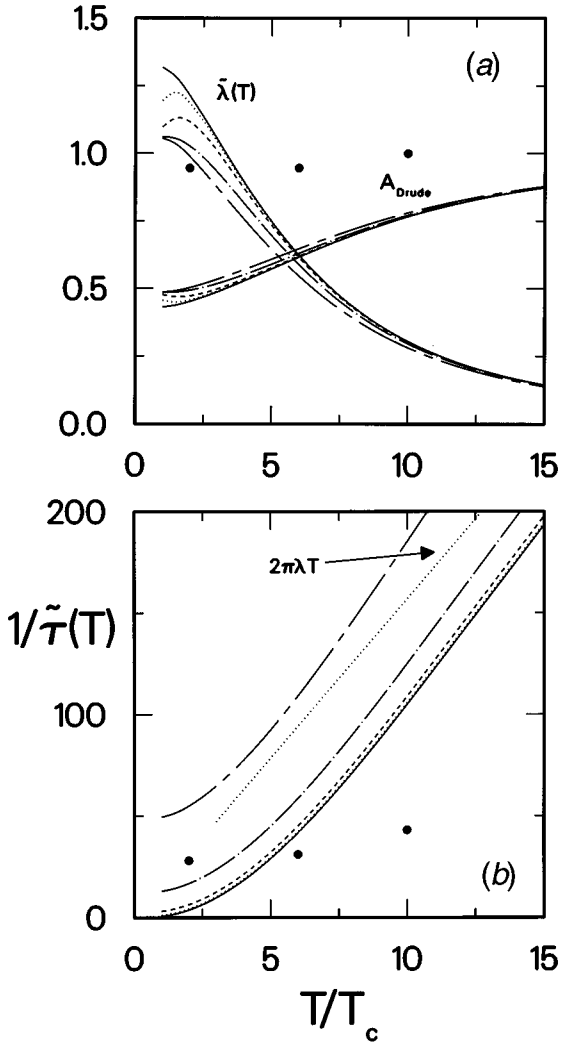

Fig. 5. (a) Normalised Drude weight (in units of $\frac{\pi}{2}\frac{ne^2}{m}$), A_{Drude} versus temperature for various impurity scattering rates, $1/\tau = 0{\cdot}01$ (solid), $1{\cdot}0$ (dotted), $5{\cdot}0$ (dashed), $25{\cdot}0$ (dot-dashed), and $100{\cdot}0$ (short-dashed long-dashed) meV. Also shown is the inferred 'coupling strength' (using equation 29) $\tilde{\lambda}(T)$ for the same impurity scattering rates. The experimental measurements of A_{Drude} from Puchkov *et al.* (1994) are indicated by the filled circles. The data are not consistent with the temperature dependence of the calculated Drude areas. (b) Fitted scattering rate $1/\tilde{\tau}(T)$ (in units of meV) versus temperature, for the same impurity scattering rates used in (a). Also shown is the high temperature result, $2\pi\lambda T$, and the experimental data of Puchkov *et al.* Their data are clearly incompatible with a coupling strength of order unity.

like normal impurities, and thus they become part of the Drude-like peak. As can be seen from the figure the influence of the actual static impurity scattering rate is minor, so analysis of conductivity data to infer $\tilde{\lambda}$ appears feasible. Thus, the temperature dependence of the Drude area gives us a good idea of the size of electron–phonon coupling. Since the area is defined to be unity at high

temperature, and approaches $1/(1+\lambda)$ at low temperatures, then if λ is small, for example, there will be very little temperature dependence in the area under the Drude-like peak. The fitted experimental results from Puchkov *et al.* (1994) are also shown in Fig. 5*a* for comparison with the theoretical curves. We have normalised their results to unity at their highest temperature, 300 K. Clearly the measured temperature dependence of the Drude area implies a very small λ.

Puchkov *et al.* (1994) actually monitored the Drude-like width as a function of temperature. In Fig. 5*b* we show the fitted scattering rate $1/\tilde{\tau}$ versus temperature, for various impurity scattering rates. Also shown is the high temperature asymptotic behaviour $1/\tilde{\tau}(T) \rightarrow 2\pi\lambda T$ obtained from (27) at high temperature. Note that asymptotic behaviour is not achieved on the scale of this plot (which extends to ≈ 450 K) so one must be cautious in using this well-known asymptotic formula. For unphysically large impurity scattering rates (long-dashed short-dashed curve) this asymptotic behaviour is never achieved. For more moderate impurity scattering rates the contribution from the phonons at least dominates by room temperature. Puchkov *et al.* (1994) analyse their data using the asymptotic behaviour noted above. (We have plotted their data points as the circles in Fig. 5*b*.) While our more detailed analysis leads to quantitative corrections their general conclusion is correct: the data are only consistent with a small electron–phonon coupling constant. We found (Marsiglio and Carbotte 1995) that the data imply a small electron–phonon coupling, $\lambda \approx 0{\cdot}1 - 0{\cdot}2$, as found in Puchkov *et al.* (1994). In this case the mechanism for superconductivity must clearly be non-conventional. This is an important result because it implies that a non-phonon mechanism drives superconductivity in this compound even though the gap clearly has s-wave symmetry, and other similarities to BCS theory, as will be noted below.

3. Superconducting State

When the electrons undergo a phase transition to the superconducting state a gap $\Delta(T)$ develops in the excitation spectrum and at zero temperature electromagnetic radiation cannot be absorbed at frequencies below the optical gap value of $2\Delta(0)$. The optical gap is twice the single-particle gap because a photon must excite an electron–hole pair, each of which is a single-particle excitation. For purposes of clarity we first review the conductivity in the superconducting state for a 'BCS' model (Bardeen *et al.* 1957; Mattis and Bardeen 1958). By this we mean some unspecified mechanism has led to superconductivity, but otherwise only electron-impurity scattering is present. There is no inelastic scattering, and thus no boson-assisted conductivity, thus simplifying the results considerably. [Technically, the gap function $\Delta(\omega) \equiv \omega\phi(\omega)/\tilde{\omega}(\omega)$ becomes independent of frequency and is a real number.] The real part of the conductivity is shown in Fig. 6 at zero temperature and near the clean limit ($1/\tau = 1$ meV) (Zimmerman *et al.* 1991). The normal state result (dashed curve) simply comes from the Drude expression (1). The superconducting state result (solid curve) consists of two parts; the remaining Drude-like component after the conductivity is gapped up to $\nu = 2\Delta(0)$, and the delta-function contribution at the origin, which takes up the missing area to fulfil the sum rule (4) and also accounts for all the key ingredients of a superconductor (zero DC resistance and Meissner–Ochsenfeld effect). The zero temperature optical gap, $2\Delta(0)$, can clearly be obtained from

such measurements. In Fig. 7 we illustrate the temperature dependence of the conductivity in the superconducting state, showing how the area is systematically removed from the gap region. Coincident with the finite frequency temperature evolution is a zero frequency delta-function (omitted in Fig. 7) which grows in strength as the temperature decreases below T_c towards $T = 0$.

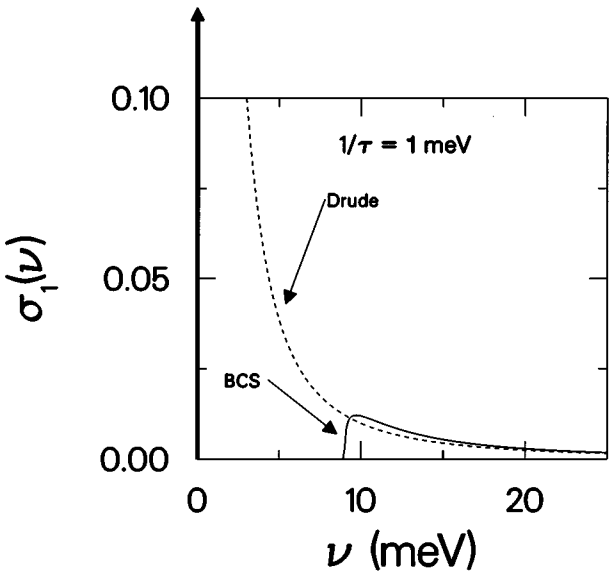

Fig. 6. A plot of $\sigma_1(\nu)$ versus ν near the clean limit ($1/\tau = 1$ meV), for the normal state (dashed curve) and the BCS superconducting state at zero temperature (solid curve plus delta-function at the origin).

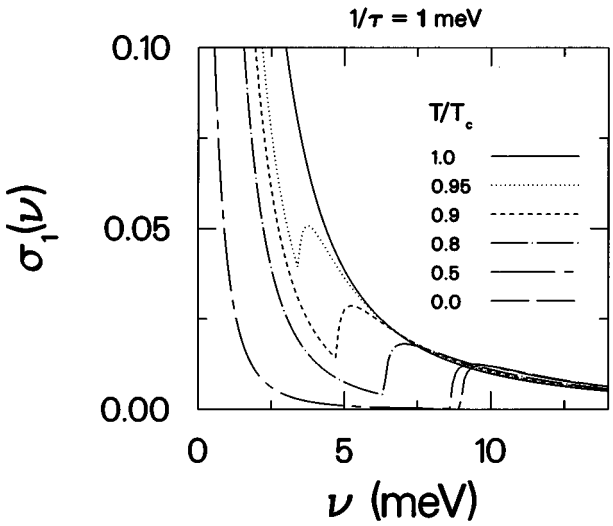

Fig. 7. Frequency dependence of $\sigma_1(\nu)$ near the clean limit ($1/\tau = 1$ meV) for various temperatures in the BCS superconducting state. The appearance of a gap is evident, even at temperatures close to T_c.

From this figure it is apparent that the gap value can be measured as a function of temperature. A Drude-like component remains for any finite temperature, which has prompted a two-fluid picture (Berlinsky *et al.* 1993; note there is a typographical error in their equations 15 and 16), consisting of a superconducting fluid (the delta-function at the origin) and a normal fluid (the low frequency conductivity at finite temperature).

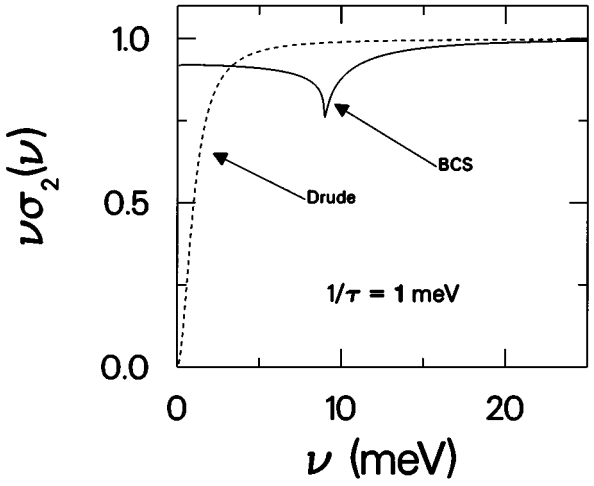

Fig. 8. A plot of $\nu\sigma_2(\nu)$ versus ν near the clean limit ($1/\tau = 1$ meV), for the normal state (dashed curve) and the BCS superconducting state at zero temperature (solid curve plus delta-function at the origin). Note the obvious signature of an optical gap, as was present in the real part (Fig. 6).

The usefulness of the imaginary part of the conductivity as a probe for the gap is much less appreciated. In Fig. 8 we show the function $\nu\sigma_2(\nu)$ versus frequency for the same parameters as in Fig. 6. It is clear that the gap can be obtained through an analysis of $\sigma_2(\nu)$ as well as $\sigma_1(\nu)$. In Fig. 9 we again show the temperature evolution as in Fig. 7, and as was the case for $\sigma_1(\nu)$ the gap feature is quite apparent for all temperatures below T_c. In addition the zero frequency limit is directly related to the London penetration depth

$$1/\lambda^2(T) = \lim_{\nu\to 0} \frac{4\pi}{c^2}\nu\sigma_2(\nu)\,. \tag{30}$$

This relation has been used recently by experimentalists (Basov *et al.* 1995) to extract the penetration depth from infrared data from an extrapolation to low frequency. This procedure is most accurate at low temperature and for the case of Fig. 9 requires measurements of points well below 1 meV at the higher temperatures shown.

Finally, it is helpful to see the dependence of the real and imaginary parts of the conductivity on impurity scattering rate. These are shown at very low temperature in the BCS limit in Fig. 10. In the real part in all cases the onset of absorption is sharp. The initial trend with increasing impurity scattering is an increase in conductivity beyond the optical gap. This is because the gap

opens in a frequency region where the normal state conductivity is still high as we move away from the clean limit [in the absolute clean limit the gap opens at a frequency where the normal state conductivity is negligible, so the gap is invisible (Kamarás *et al.* 1990)]. However, as the scattering rate increases still further, the overall scale of the conductivity decreases, so the conductivity near the optical gap decreases, as is evident from Fig. 10*a*. In the imaginary part (Fig. 10*b*) this decrease in scale is most evident, and of course indicates that the penetration depth increases with impurity scattering. Furthermore, the cusp-like minimum near the optical gap becomes very smooth as the impurity scattering rate increases, so that the gap is far less evident in the dirty limit than for a low impurity scattering rate.

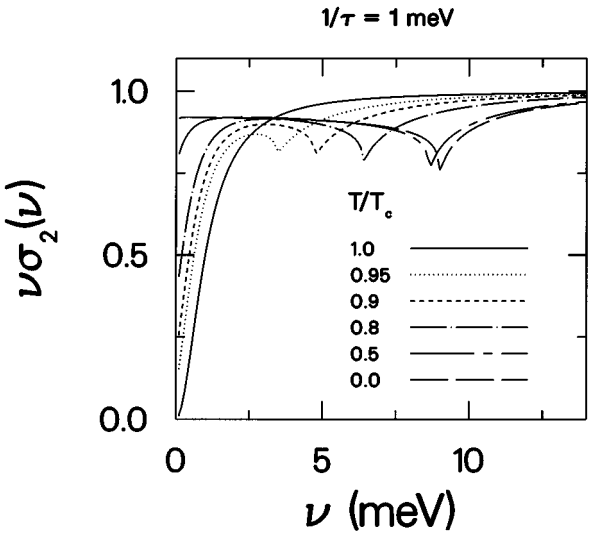

Fig. 9. Frequency dependence of $\nu\sigma_2(\nu)$ near the clean limit ($1/\tau = 1$ meV) for various temperatures in the BCS superconducting state. The appearance of a gap is evident in the imaginary part of the conductivity as well, even at temperatures close to T_c.

The BCS results presented above show fairly sharp cusp-like features at frequencies corresponding to the optical gap, particularly for small values of $1/\tau$. However, as we have already seen in the normal state, inelastic scattering processes introduce damping effects, so that some of these sharp features may become somewhat smeared. We turn now to a discussion of the quantitative effects of inelastic scattering processes, again in the context of the oxide superconductor $Ba_{1-x}K_xBiO_3$ (Marsiglio *et al.* 1996). In Fig. 11 we show the real part of the conductivity versus frequency for various temperatures below T_c in the (*a*) superconducting and (*b*) normal states. For the purposes of illustration we have adopted the clean limit ($1/\tau = 0$) as in Fig. 3 so that the Drude-like parts come from thermally populated phonons. This is clear in both frames: the Drude part narrows as the temperature is lowered. Clearly the suppression is more pronounced in the superconducting state than in the normal state due to the formation of the condensate and the corresponding reduction in the normal state fluid component. At zero temperature in the superconducting state the absorption edge starts at

$2\Delta(0) = 10 \cdot 4$ meV. The phonon spectrum (Fig. 2) extends down to zero frequency, otherwise this edge would be offset further by the minimum phonon energy. In this case, with no impurity scattering, it is virtually impossible to observe the optical gap value (compare Fig. 6 or 7). In the normal state the absorption edge is at zero frequency (at $T = 0$) so that superconductivity has effectively resulted in a $2\Delta(0)$ frequency shift in the phonon-assisted contribution (of course there is an additional delta-function at the origin). Otherwise the two results are similar; in particular both display some modulation of the phonon-assisted contribution which reflects to some extent the underlying phonon spectrum (Fig. 2).

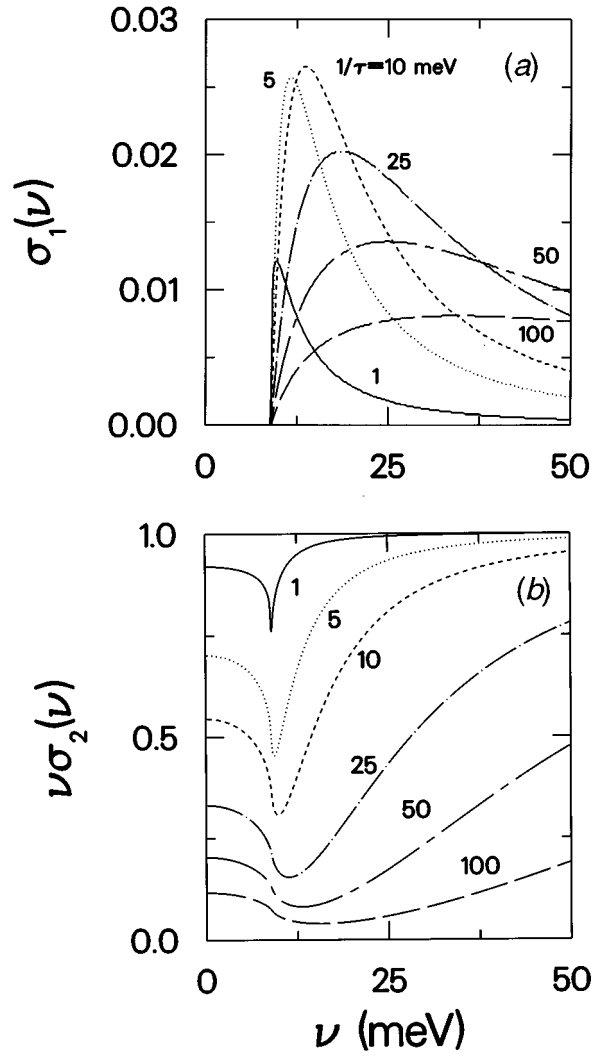

Fig. 10. (*a*) A plot of $\sigma_1(\nu)$ versus ν in the zero temperature BCS superconducting state for the various impurity scattering rates indicated. The absorption onset at $2\Delta(0)$ remains sharp independent of the scattering rate. A delta-function contribution (not shown) is also present at the origin. (*b*) Same as in (*a*) except for the frequency times the imaginary part of the conductivity. The optical gap is a little less evident in the dirty limit.

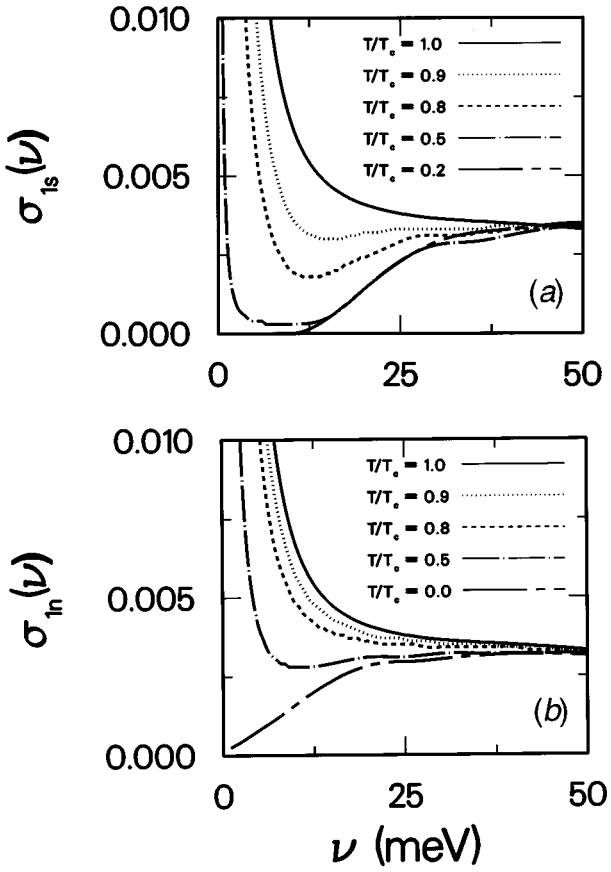

Fig. 11. Real part of the conductivity versus frequency for various temperatures in (a) the superconducting state and (b) the normal state. These results are for the clean limit, $1/\tau = 0$, so only inelastic scattering is present, provided by the model phonon spectrum for BKBO (Fig. 2). The presence of a superconducting gap is not obvious in (a).

When even a small amount of impurity scattering is included the situation changes significantly. In Fig. 12 we show results for the same phonon spectrum, but with additional impurity scattering present ($1/\tau = 2$ meV). The gap edge is now clearly visible, even at finite temperatures, due to impurity-assisted absorption processes.

As the previous two figures and Fig. 3 indicate, structure is visible in the conductivity in the phonon energy region (0–70 meV) for the lowest temperatures shown. This structure in the phonon region was observed many years ago in superconducting Pb (Joyce and Richards 1970; Farnworth and Timusk 1974). With the addition of impurities this structure is smeared out in the normal state. However, in the superconducting state the structure is restored, even in the dirty limit. As the coupling strength increases, the structure in the conductivity (as in the tunneling density of states) becomes more pronounced. Puchkov *et al.* (1994) noted the absence of structure in their measurements, which they took as evidence for a lack of electron–phonon coupling. In Fig. 13a we plot the

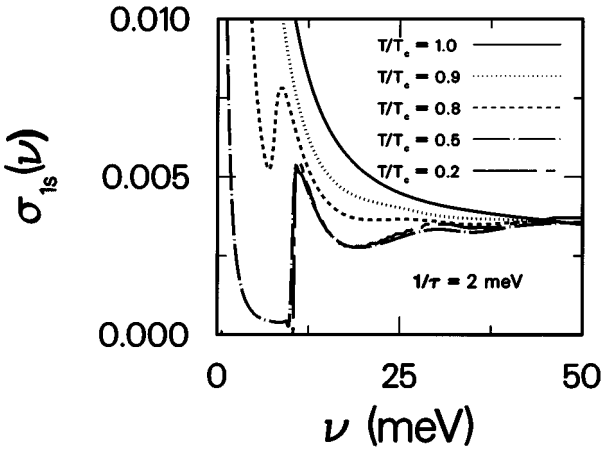

Fig. 12. As in Fig. (11*a*), the real part of the conductivity versus frequency for various temperatures in the superconducting state, but with $1/\tau = 2$ meV. Now the presence of a superconducting gap is evident.

real part of the conductivity in the clean limit for (i) the normal state at T_c (solid curve), (ii) the normal state at $T/T_c = 0{\cdot}1$ (dotted curve), and (iii) the superconducting state at $T/T_c = 0{\cdot}1$ (dashed curve), using our model spectrum, Fig. 2 (Marsiglio and Carbotte 1995). This plot serves to clarify some of the results of previous figures. It is readily seen that even the structure is shifted by the optical gap in going from the normal to superconducting state. However, we should emphasise that the normal state conductivity is not usually measured below T_c. Rather it is the normal state conductivity at T_c (solid curve) that is measured and, as Fig. 13*a* indicates, the structure present is barely discernable. This makes the frequency *shift* in structure unobservable. In Fig. 13*b* we show the same quantities, now with an impurity scattering rate of $1/\tau = 25$ meV. While no structure is observable in the normal state either at $T/T_c = 1{\cdot}0$ or $0{\cdot}1$, it is evident in the superconducting state, albeit far less than in the clean limit. It is not likely that such structure could be discernable from the measurements of Puchkov *et al.*, should it be present. One must also keep in mind that in the presence of normal impurity scattering, the structure is *only* observable in the superconducting state, and this is due to the opening of a gap, followed by a singular density of states. Any intrinsic material property that gives rise to a smearing of this singularity will also smear the phonon structure, thus rendering it unobservable.

We now turn to a discussion of the imaginary part of the conductivity in the presence of inelastic scattering (Marsiglio *et al.* 1996). In Fig. 14*a* we plot $\nu\sigma_2(\nu)$ versus ν for the $Ba_{1-x}K_xBiO_3$ spectrum with $\lambda = 1$ and $T_c = 29$ K as discussed previously. The curves are plotted in the clean limit, i.e. $1/\tau = 0$, so the real conductivity plot has already been given in Fig. 11. The very sharp Drude-like peak present at low temperatures in the real part of the normal state conductivity manifests itself in the imaginary part of the conductivity as a sharp inverted Drude-like minimum near the origin, as is visible in the lower left portion of Fig. 14*a*. The solid curve is for $T/T_c = 0{\cdot}99$ while the dotted curve,

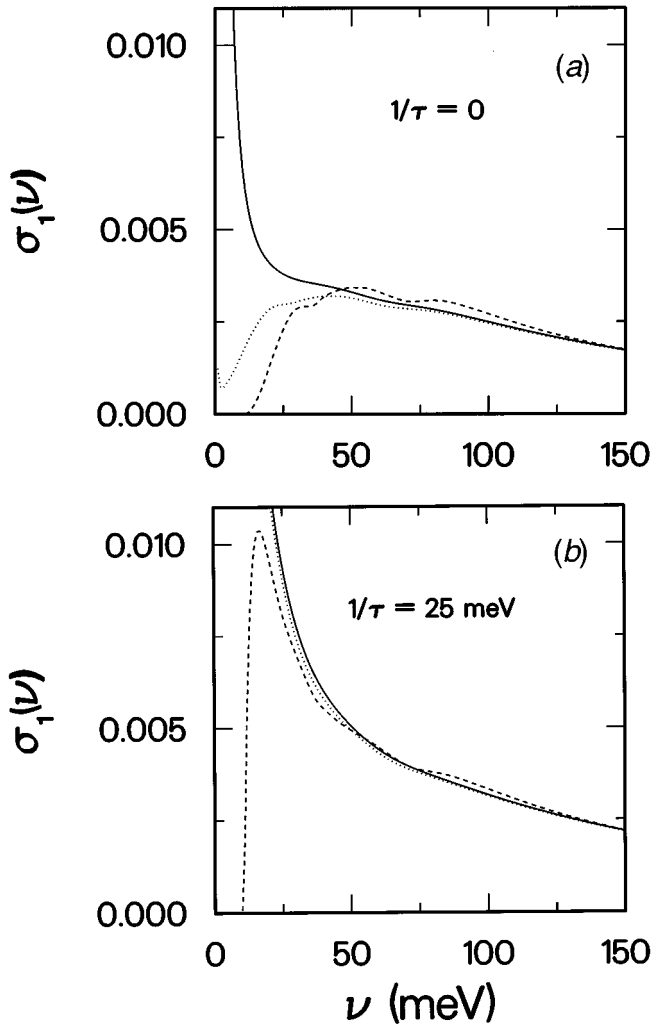

Fig. 13. Real part of the conductivity versus frequency for (*a*) $1/\tau = 0$ and (*b*) $1/\tau = 25$ meV, using the BKBO spectral density. Results are shown for the normal state at T_c (solid curve), normal state at $T/T_c = 0{\cdot}1$ (dotted curve), and for the superconducting state at $T/T_c = 0{\cdot}1$ (dashed curve).

which is almost indistinguishable from the solid curve, is for the normal state at the same temperature. The difference occurs near the origin (not shown) as the normal state curve goes to zero, whereas the superconducting state curve has an intercept related to the penetration depth by equation (30). The results at lower temperature show the effects of inelastic scattering most clearly (compare with Fig. 8 or 9). First, the sharp structure at $\nu = 2\Delta \approx 10{\cdot}4$ meV is absent. However, in this case there is no BCS reference, as in the clean limit the corresponding result would be a constant at value unity (see Fig. 10*b*). The lack of sharp structure is also consistent with the lack of an abrupt onset in the real part (see Fig. 11) since the two are related by a Kramers–Kronig relation.

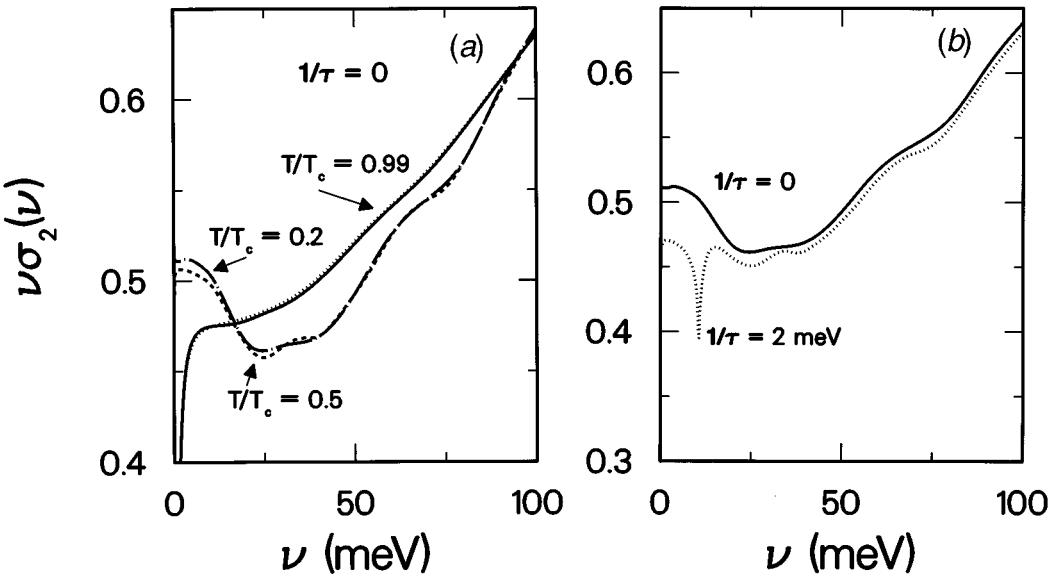

Fig. 14. A plot of $\nu\sigma_2(\nu)$ versus frequency, using the BKBO spectrum as in Fig. 13. In (a) we use $1/\tau = 0$ (clean limit) and plot the results for the indicated temperatures. The solid (dotted) curve is for the superconducting (normal) state at $T/T_c = 0{\cdot}99$. Inelastic scattering has smoothed the BCS cusp-like minimum at $\nu = 2\Delta_0 \approx 10{\cdot}4$ meV. In (b) we focus on the low temperature results ($T/T_c = 0{\cdot}2$) and show the effect of a small amount of impurity scattering. The cusp-like minimum at 2Δ is clearly restored.

Another difference is the presence of structure over a frequency range representative of the phonon energies in the $\alpha^2F(\omega)$ spectrum, as occurs in the real part of the conductivity. This leaves open the possibility for the determination of $\alpha^2F(\omega)$ by infrared spectroscopy with the imaginary part of the conductivity.

Finally another clear difference occurs in the zero frequency limit, where at low temperatures the intercept is approximately $0{\cdot}5$, i.e. half of the London limit. This is due to phonon renormalisation effects which, for the most part, amount to a $1 + \lambda$ enhancement of the mass.

In Fig. 14b we show what occurs when the impurity scattering rate is nonzero. A cusp-like minimum is present, as was the case in the BCS limit (Fig. 10b). Secondly the penetration depth, given by the zero frequency limit of $\sigma_2(\nu)$ (see equation 30), has increased with the addition of impurities, as discussed in the BCS limit.

To see the effect of coupling strength on the low frequency imaginary part of the conductivity, in Fig. 15 we first plot the real part of the conductivity versus frequency with (a) $1/\tau = 2$, and (b) $1/\tau = 25$ meV, for various coupling strengths as indicated (the Coulomb repulsion μ^* is adjusted in each case so that $T_c = 29$ K), and the quantity $\nu\sigma_2(\nu)$ in (c) and (d) for the same impurity scattering rates as in (a) and (b), respectively. The decrease in scale with increasing coupling strength is evident in all four figures. The real part of the conductivity has a sharp absorption onset at 2Δ independent of the coupling strength. For the imaginary part the depth and sharpness of the minimum associated with the optical gap decreases as the coupling strength increases. The

onset in the real part and the minimum in the imaginary part also shift slightly to higher frequency, as expected since the zero temperature gap increases with increasing coupling strength. At higher frequencies phonon structure becomes more noticeable in all cases as coupling strength increases.

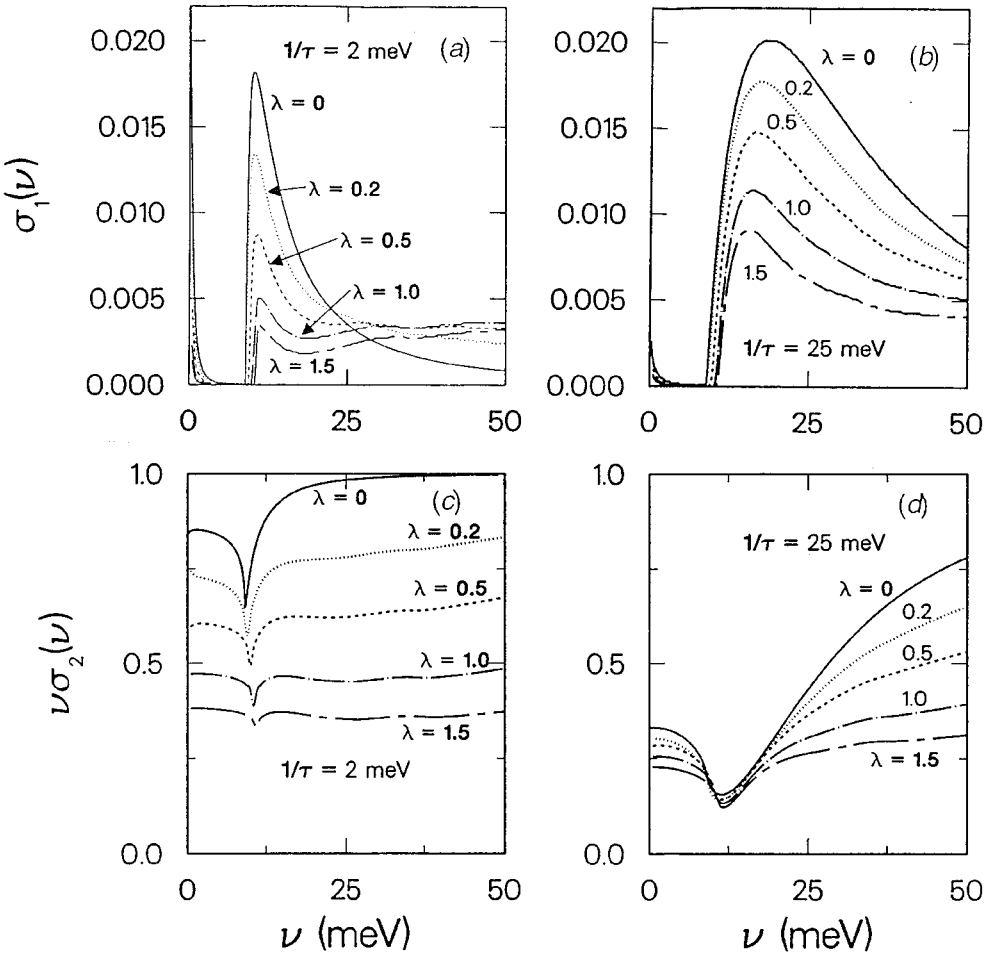

Fig. 15. Real part (a) and (b) and imaginary part (c) and (d) of the conductivity at essentially zero temperature ($T/T_c = 0{\cdot}3$) with $1/\tau = 2$ meV (a and c) and $1/\tau = 25$ meV (b and d). In all cases we have used the BKBO spectrum scaled to give the designated value of λ, while T_c is held fixed at 29 K by adjusting μ^*. Increased coupling strength suppresses both $\sigma_1(\nu)$ and $\nu\sigma_2(\nu)$ and broadens the minimum in the latter at 2Δ. Note that 2Δ increases slightly as the coupling strength is increased.

We earlier discussed Drude-like fits to the real part of the conductivity in the normal state (see Fig. 4). A similar procedure has been implemented for the imaginary part of the conductivity (Marsiglio *et al.* 1996) and the results are shown in Fig. 16. As before the Drude fits are given by dotted curves and the full electron–phonon results by solid curves. Similar plots would work with non-zero impurity scattering. In units of ne^2/m, $\nu\sigma_2(\nu)$ as modelled by the complex Drude form (see equation 25),

$$\sigma_{\mathrm{Drude}} \equiv \frac{ne^2}{m}\,\frac{1}{1+\tilde{\lambda}}\,\frac{\tilde{\tau}}{1-i\nu\tilde{\tau}}\,, \tag{31}$$

will saturate at high frequencies to a value of $1/(1+\tilde{\lambda})$, which is $0{\cdot}43$ for the chosen parameters at T_c. This saturation is seen very clearly in the plots. As the temperature is increased to $T/T_c = 5$, the inelastic scattering increases significantly, consistent with the real conductivity results. Note that $\lim_{\nu\to\infty} \nu\sigma_2(\nu) = 1$ in the full calculation (in units of ne^2/m). Thus, one could use $\nu\sigma_2(\nu)$ data to determine $\tilde{\lambda}$ and $\tilde{\tau}$ independently from the low frequency fit and from the infinite frequency limit.

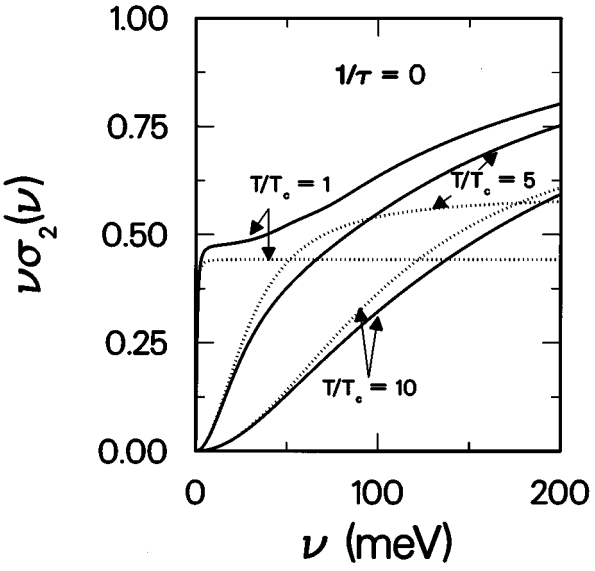

Fig. 16. A plot of $\nu\sigma_2(\nu)$ versus frequency for $1/\tau = 0$ (clean limit) in the normal state, using the BKBO spectrum, showing the excellent agreement at low frequency between the full calculations (solid curves) and the Drude fits, as in Fig. 4.

We have already explained how Puchkov *et al.* (1994) used the real part of the conductivity in samples of $Ba_{1-x}K_xBiO_3$ to conclude that this material cannot be a conventional electron–phonon superconductor with coupling constant value $\lambda \approx 1$. This conclusion was further reinforced by the calculations already presented (Marsiglio and Carbotte 1995), and by examining the imaginary part (Marsiglio *et al.* 1996). The plot in Fig. 17 summarises some of the main conclusions concerning the imaginary part. The experimental spectra were obtained using a Kramers–Kronig analysis of the reflectivity spectra measured from 25 cm^{-1} to 40,000 cm^{-1} (Puchkov *et al.* 1994) and extrapolated at high frequency in such a way as to match ellipsometric measurements on the same crystal. The minimum at approximately 12 meV is striking evidence of an s-wave order parameter in the $Ba_{1-x}K_xBiO_3$ system. Similar results for other dopant concentrations (and hence T_c values) have also been obtained (Puchkov *et al.* 1996). This conclusion has been reinforced by complementary work by Jiang and Carbotte (1996*a*) where they investigate the behaviour of the imaginary part of the conductivity

for a superconductor with order parameter of d-wave symmetry and find that no minimum occurs in $\nu\sigma_2(\nu)$ at 2Δ. These results will be discussed further in the next section.

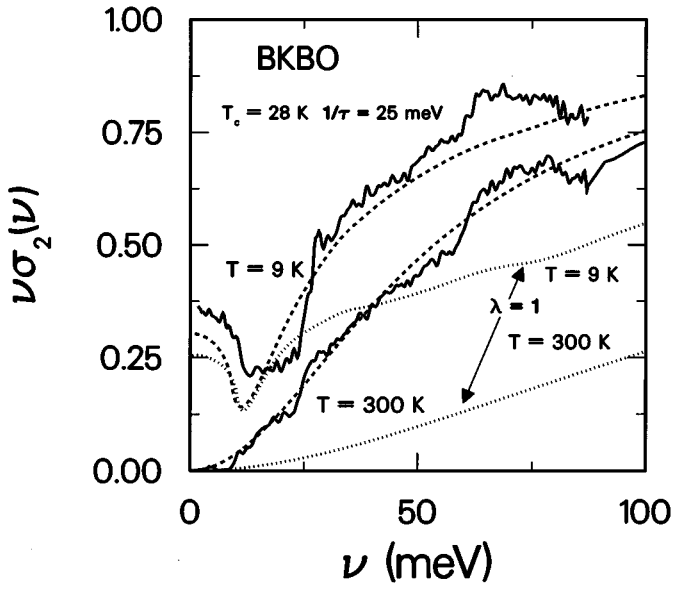

Fig. 17. Measured $\nu\sigma_2(\nu)$ versus frequency at $T = 9$ K and at $T = 300$ K (solid curves) (Marsiglio *et al.* 1996). Also shown are the theoretical fits, using the BKBO spectrum, scaled so that $\lambda = 0{\cdot}2$ (dashed curves). Here T_c is kept fixed to the experimental value with a negative μ^*. Finally, theoretical fits are also shown with $\lambda = 1$ (dotted curves). The latter curves are clearly incompatible with the experimental results.

Given the normalisation of the experimental data discussed above, Fig. 10*b* makes it clear that a considerable amount of impurity scattering is required to achieve a qualitative agreement between theory and experiment. This observation is also consistent with the analysis of the real part of the conductivity, although in that instance a 'mid-infrared contribution' of unknown origin was subtracted from the data first. Then Fig. 15*b* shows that for λ of order unity, the large amount of inelastic scattering present at relatively high frequencies (≈25–50 meV) will reduce the imaginary part of the conductivity, in disagreement with experiment. This disagreement will be even more significant at higher temperatures.

Theoretical curves are also plotted in Fig. 17 to more clearly illustrate these remarks. As a 'good' representative fit we show results at the two temperatures using a reduced $\alpha^2F(\omega)$ for $Ba_{1-x}K_xBiO_3$ with $\lambda = 0{\cdot}2$ (dashed curves). We have used $1/\tau = 25$ meV, a value which is consistent with that obtained experimentally from $\sigma_1(\nu)$ (Puchkov *et al.* 1994, 1996). It is clear that the fit is quantitatively good. For comparison we also show the result using the full spectrum, i.e. with $\lambda = 1$. It is obvious that such a fit is poor, and given our previous results, the reader can appreciate that no amount of parameter adjustment will yield good agreement with the data *at both temperatures* while retaining λ of order unity. This general result is, of course, consistent with the conclusion inferred from the real part of the conductivity (Puchkov *et al.* 1994; Marsiglio and Carbotte 1995).

The analysis of the imaginary part, however, has the advantage that no data subtraction is required before the analysis. It has the disadvantage that a high frequency scale is required to normalise the experimental data shown in Fig. 17.

We should briefly summarise the consequences of an s-wave order parameter along with an inelastic scattering mechanism. Within the BCS model (no inelastic scattering) the real part of the conductivity shows an onset of absorption at the optical gap, 2Δ. The imaginary part of the conductivity shows a cusp-like minimum at the same frequency, which is most pronounced for a low impurity scattering rate. In the presence of impurity scattering strong coupling effects modify the results by smearing the gap minimum, and renormalising the low frequency behaviour through a renormalisation $1/\tilde{\tau} \rightarrow \dfrac{1/\tau}{1+\lambda}$. [We have shown that the renormalisation is actually $1/(1+\tilde{\lambda})$. However, $\lim_{T\rightarrow 0}\tilde{\lambda}(T) = \lambda$. Also, note that the first order effect of adding an additional inelastic scattering process (electron–phonon coupling) to an elastic scattering process (impurity scattering) is to *reduce* the overall scattering rate (at low temperatures). This occurs because the inelastic scattering reduces the spectral weight of the quasiparticle undergoing the scattering.] In addition, structure is apparent in the phonon region.

In the clean limit only inelastic scattering occurs and there is no structure in $\nu\sigma_2(\nu)$ at twice the gap value because absorption across the gap can only proceed through a phonon-assisted mechanism needed to absorb the necessary momentum and energy. Thus the onset in the real part of the conductivity is smooth since the density of phonon states usually has an ω^2 dependence at low frequency. When impurities are added, a qualitative change occurs because impurity-assisted absorption can now set in quite abruptly at 2Δ. This manifests itself in the imaginary part of the conductivity as a sharp cusp-like minimum in $\nu\sigma_2(\nu)$.

Application of our calculations to the specific case of $Ba_{1-x}K_xBiO_3$ allows us to conclude that this system is an s-wave superconductor. On the other hand further analysis suggests that the superconductivity is not phonon-mediated as others have concluded. The data are consistent with an electron–phonon mass enhancement parameter of about $\lambda \approx 0{\cdot}2$ and *inconsistent* with larger values of order unity suggested in the literature and required to produce $T_c \approx 30$ K.

4. The Cuprate Superconductors

Untwinned single crystals of $YBaCu_3O_{7-x}$ (YBCO) exhibit a very large inelastic scattering rate in the normal state of the order of a few T_c at a temperature $T = T_c$ (Iye 1992). This indicates that some inelastic scattering mechanism should be included as a fundamental characteristic of the cuprate superconductors if their properties are to be properly understood. That this scattering is primarily inelastic is inferred from the strong temperature dependence of the resistivity above T_c. Extrapolation to below T_c (and measurements on related lower T_c compounds) show that the residual resistivity is quite low, which leads to a second important feature—that the cuprates have very little impurity scattering, i.e. they are in the clean limit. This conclusion is further justified in the superconducting state since the relevant length scale is the coherence length, which is known to be very short.

In addition it has been established with several experimental techniques that the superconducting gap has d-wave symmetry with nodes on the Fermi surface (Scalapino 1995). We will not review these varied results; instead we will focus on one possible mechanism which leads to both strong inelastic scattering and a d-wave symmetry order parameter, the nearly antiferromagnetic Fermi liquid model (NAFLM) (Millis *et al.* 1990; Monthoux and Pines 1993). The NAFLM is very similar to a phonon mechanism, except that the boson in this case is an antiferromagnetic spin fluctuation. Thus the spin susceptibility plays the role of the electron–phonon spectral function, and leads to both inelastic scattering and pairing. The spectral function is modelled by the simple form (Jiang *et al.* 1996)

$$\alpha^2 F(\omega) = b^2 \frac{\omega/\omega_{\rm sf}}{1 + (\omega/\omega_{\rm sf})^2}\,. \tag{32}$$

Here $\omega_{\rm sf}$ sets the scale for typical spin fluctuations—for various reasons we take it to be $\omega_{\rm sf} \approx 30$ meV (Schuttler and Norman 1996). The parameter b^2 is purely phenomenological, and will be determined by the requirement that $T_c \approx 100$ K. A cutoff for this spectrum is also required, which we take to be 400 meV. The ratio $T_c/\omega_{\rm sf}$ is indicative of the coupling strength. Here it is $0{\cdot}3$, which is substantial (a similar measure of superconducting Pb gives $0{\cdot}13$). Another important difference with phonon theories is that the spectral function is linear in frequency at low frequency rather than quadratic.

The cuprate superconductors are also quasi-two-dimensional. Thus the Fermi surface is modelled by a cylinder, so that the problem is effectively two dimensional, with a circular Fermi surface in the two-dimensional copper oxide Brillouin zone. In this discussion we also adopt a single band model, though other complications arise, in particular for YBCO, where 'chain' bands also exist (Atkinson and Carbotte 1995). Further we adopt a separable model for the pairing interaction, which leads to the simplified angular dependence of the superconducting gap

$$\Delta(\theta) = \Delta \cos 2\theta\,, \tag{33}$$

where θ is the angle in momentum space with origin the x-axis (along a nearest-neighbour bond direction). Then the gap has zeros along the $\theta = \pm 45^\circ$ and $\theta = \pm 135^\circ$ directions. Inelastic scattering can be incorporated in a straightforward way. The relevant Eliashberg equations (see the following paper) will have a separable spectral function $g \cos(2\theta) \cos(2\theta') \alpha^2 F(\omega)$ in the gap channel and, for simplicity, an isotropic spectral function $\alpha^2 F(\omega)$, in the frequency renormalisation channel. The phenomenological parameter g accounts for the possible differences in the characteristic inelastic scattering form in the different channels of Eliashberg theory. In general it will differ somewhat from unity, but its precise value does not have a qualitative effect on the results.

We have avoided writing down the full expressions for the Eliashberg equations and for the conductivity with the anisotropic gap, equation (33). These expressions and further discussion can be found in Carbotte *et al.* (1995) and Jiang and Carbotte (1996*b*). We note that the results presented below are all obtained with $T_c = 100$ K, $\omega_{\rm sf} = 30$ meV, and $g = 0{\cdot}8$, and utilise the spectral function (32).

In Fig. 18*a* we show results for the real part of the conductivity in the superconducting state, in the clean limit (Jiang *et al.* 1996). All finite temperature results display a Drude-like peak at zero frequency, as was the case for an s-wave gap (Fig. 11). Similarly there is no clearly identifiable signature of a superconducting gap. Here, however, there is an additional reason for the lack of a signature, which is the d-wave symmetry of the gap parameter, which has nodes on the Fermi surface. Thus, the single-electron density of states is non-zero for all frequencies and, within BCS theory (Zhou and Shultz 1992), has only a logarithmic singularity at a frequency of about twice the maximum gap value on the Fermi surface. This singularity is much more easily smeared by finite temperature and strong coupling effects, compared to the similar s-wave gap.

In addition the linear low frequency behaviour of the spectral function (32) tends to smear the cross-over region from Drude-like to boson-assisted. This cross-over leads to a well-defined minimum in Fig. 11*a*, for example, which is present in Fig. 18*a* as well, but more difficult to see.

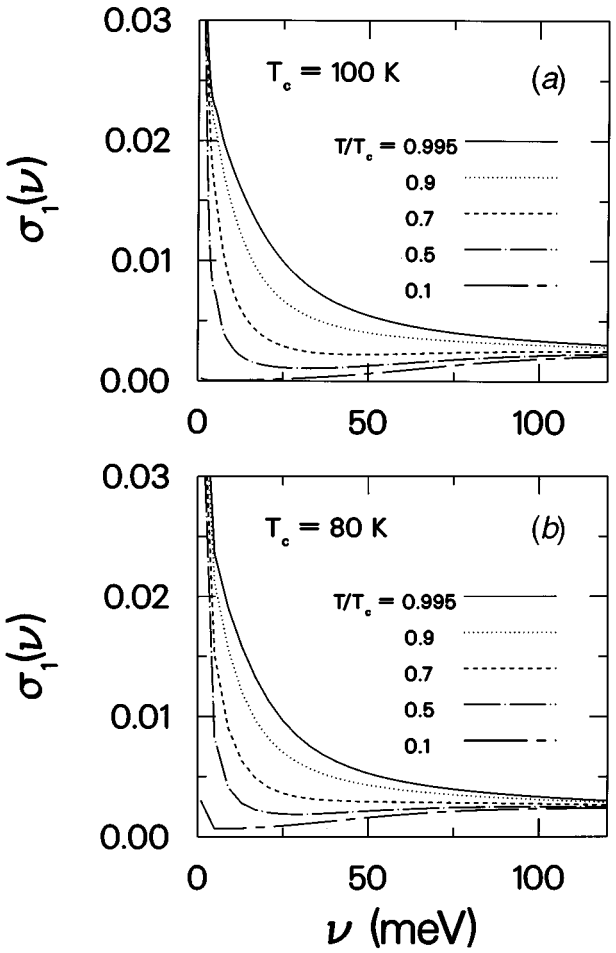

Fig. 18. Real part of the conductivity versus frequency for various temperatures in a d-wave superconducting state (*a*) for the clean limit and (*b*) with sufficient impurity scattering to reduce T_c to 80 K (Jiang *et al.* 1996). In either case there is no optical gap.

The impact of the d-wave order parameter is more evident in comparing Fig. 18*b* to Fig. 12. In Fig. 18*b* we have included impurity scattering which, in the case of an s-wave order parameter (Fig. 12), led to an abrupt onset in the real part of the conductivity at a frequency equal to twice the value of the

single-electron gap. Such behaviour is clearly absent in Fig. 18*b*, even though impurity scattering is present and sufficiently strong that the critical temperature is reduced from 100 K to 80 K.

Similar remarks apply to the imaginary part of the conductivity, as Figs. 19*a* (clean limit) and 19*b* (impurity scattering present) show (Jiang *et al.* 1996), when compared to the s-wave case (see, for example, Fig. 14). Here, particularly for Fig. 19*b*, there is no cusp-like feature at the optical gap frequency. Such a result is in qualitative agreement with experiments on YBCO (Jiang *et al.* 1996), and lends support to the existence of a gap function with nodes on the Fermi surface.

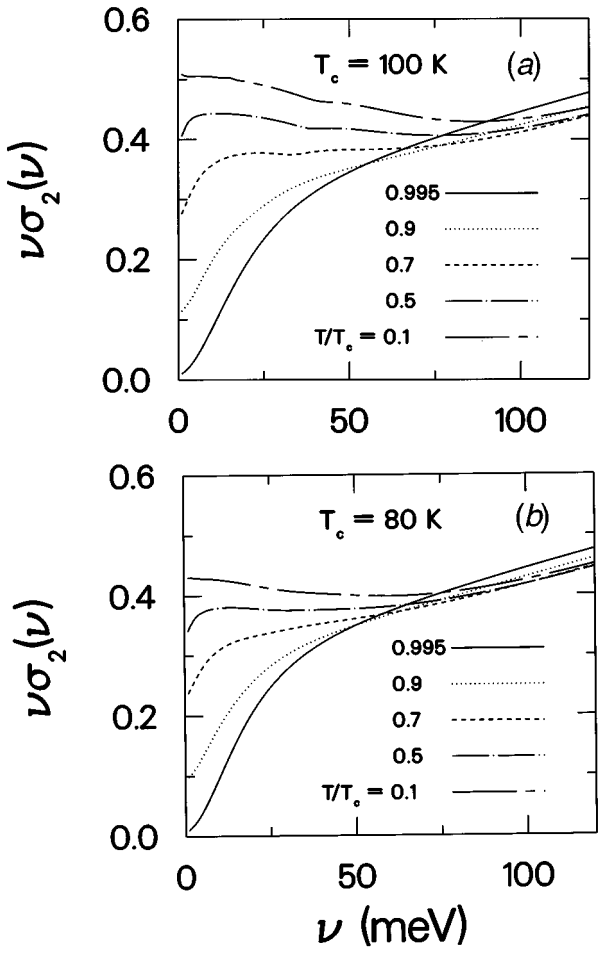

Fig. 19. Frequency times the imaginary part of the conductivity versus frequency for various temperatures in a d-wave superconducting state (*a*) for the clean limit and (*b*) with sufficient impurity scattering to reduce T_c to 80 K (Jiang *et al.* 1996), as in Fig. 18. Here as well there is no indication of an optical gap.

So far we have discussed the real and imaginary parts of the conductivity. It is useful to examine the frequency-dependent transport scattering rate as defined by equation (2) for the superconducting state. Even for a simple Drude model,

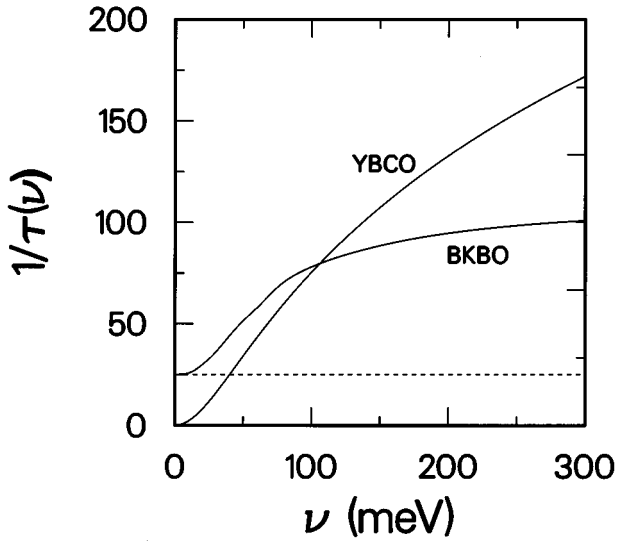

Fig. 20. Conductivity-derived scattering rate $1/\tau(\nu) \equiv \mathrm{Re}\ (1/\sigma(\nu))$ versus frequency in the normal state for pure elastic scattering (dashed line), combined elastic and inelastic scattering (BKBO spectrum with $\lambda = 1$), and pure inelastic scattering using the spin fluctuation spectrum (32) appropriate to YBCO. Because of the difference in spectral function frequency scales, the result for YBCO continues to rise with frequency, even at 300 meV.

where $1/\tau(\nu)$ so defined would be a constant in the normal state (equation 1), it would acquire frequency dependence in the superconducting state. When inelastic scattering is included, further frequency dependence is expected, even in the normal state. To illustrate this we show in Fig. 20 normal state results for pure elastic scattering ($1/\tau = 25$ meV) (dashed line), for combined elastic and inelastic scattering, using the spectral function for BKBO (solid curve as labelled) and for pure inelastic scattering, using the spin fluctuation model for YBCO (equation 32) (other solid curve). In the BKBO case it is clear that the scattering rate has almost saturated after an initial rapid rise with increasing frequency. On the other hand, because of the frequency range of the spin fluctuation spectrum, the result for YBCO continues to rise, and in fact appears quasilinear over a wide range of frequency. Scattering rates thus obtained can be compared with the inverse quasiparticle lifetime (Dolgov *et al.* 1991; Shulga *et al.* 1991), defined in (21) through the single-particle self-energy. As was the case with the temperature dependence, the frequency dependence of the inverse lifetime is largely determined by the frequency dependence of the spectral function. In fact, at $T = 0$ the inverse lifetime is given as a simple function of $\alpha^2 F(\omega)$:

$$\Gamma(\omega) = 1/\tau + 2\pi \int_0^{\omega} d\Omega \alpha^2 F(\Omega)\,. \tag{34}$$

Thus, for a Debye model, with $\alpha^2 F(\omega) \propto \omega^2$ at low frequency, then (with no impurity scattering)

$$\Gamma_{\mathrm{Debye}}(\omega) \approx \omega^3 \tag{35}$$

as $\omega \to 0$. It is also apparent from (34) that for a frequency large compared with the Debye frequency the inverse lifetime approaches a constant. For the marginal Fermi liquid spectral function, (13),

$$\Gamma_{\rm MFL}(\omega) \approx \omega\,, \tag{36}$$

while for the NAFLM, (32),

$$\Gamma_{\rm NAFLM}(\omega) \approx \omega^2 \tag{37}$$

for low frequency.

In Fig. 21 we show results for $\Gamma(\omega)$ at zero temperature in the normal state, for the same cases as discussed in Fig. 20. The two sets of results are qualitatively similar, but quantitatively very different. Fig. 21 (the inverse quasiparticle lifetime) saturates much more rapidly with frequency than does the scattering rate as defined through the optical conductivity, (2).

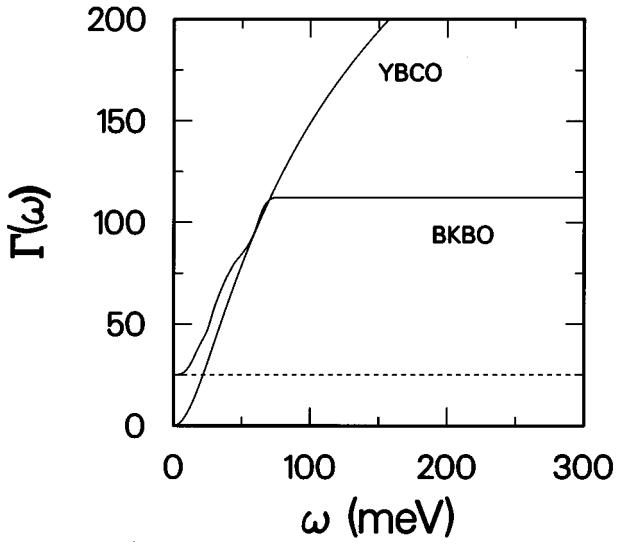

Fig. 21. Inverse quasiparticle lifetime in the normal state (34) for the three cases given in Fig. 20. The increase with frequency is considerably more abrupt than in the scattering rate (Dolgov *et al.* 1991).

Extension to the superconducting state will be discussed at length in the following paper. Here we show some results for the scattering rate as obtained from equation (2). In Fig. 22 we show $1/\tau(\nu)$ versus frequency for a BCS model with an impurity scattering rate (a) $1/\tau = 2$ meV and (b) $1/\tau = 25$ meV. The horizontal dotted line is the simple normal state result shown for reference. The other curves are for the various temperatures indicated in the figure caption. Note that the temperature dependence of the gap is discernable in such a plot. To see what modifications inelastic scattering brings about, we show results for the BKBO spectrum in Fig. 23 for (a) the clean limit $(1/\tau = 0)$ and (b) $1/\tau = 25$ meV, again for the temperatures as indicated. As occurred in the real

and imaginary parts of the conductivity, in the clean limit there is no clear signature for a gap. However, in the presence of elastic impurity scattering the gap is clearly visible at low temperatures, and to a lesser degree apparent even at higher temperatures. Finally, we examine $1/\tau(\nu)$ for the superconducting state with a d-wave order parameter, with inelastic scattering present. In Fig. 24 we show the result obtained with the spin fluctuation spectrum in (a) the clean limit, and (b) with elastic impurity scattering present. In either case there is no clear indication of a gap, as expected for a d-wave superconducting state.

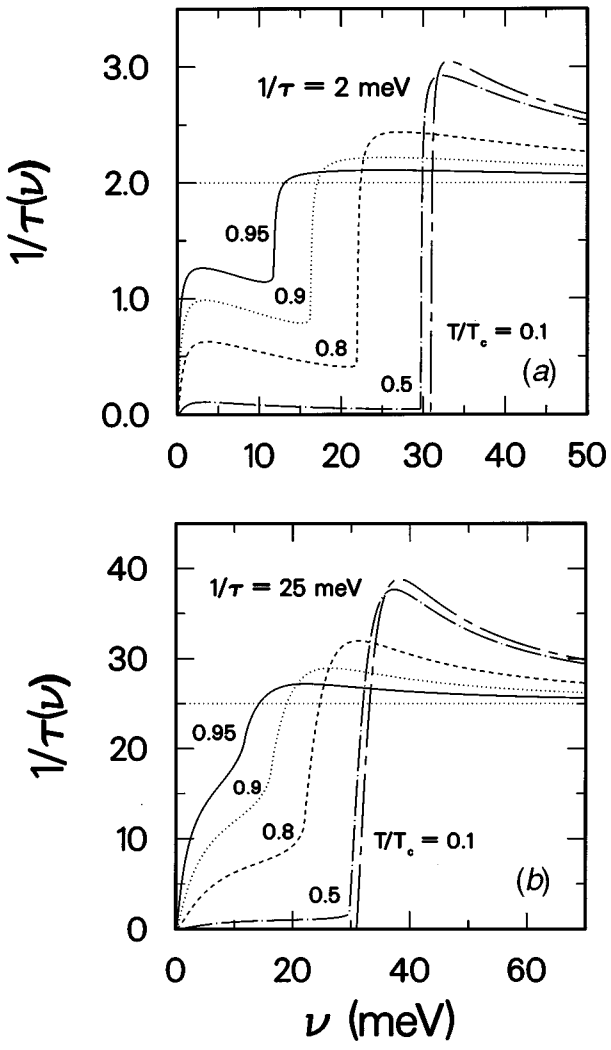

Fig. 22. Conductivity-derived scattering rate $1/\tau(\nu)$ versus frequency in the BCS s-wave superconducting state for (a) $1/\tau = 2\,\text{meV}$ and (b) $1/\tau = 25\,\text{meV}$. An abrupt onset of absorption at the optical gap at temperatures near T_c is more apparent in (a) than in (b). The temperatures are $T/T_c = 0{\cdot}95$ (solid), $T/T_c = 0{\cdot}9$ (dotted), $T/T_c = 0{\cdot}8$ (dashed), $T/T_c = 0{\cdot}5$ (dot-dashed) and $T/T_c = 0{\cdot}1$ (short-dash–long dashed). The horizontal dotted line indicates the normal state result.

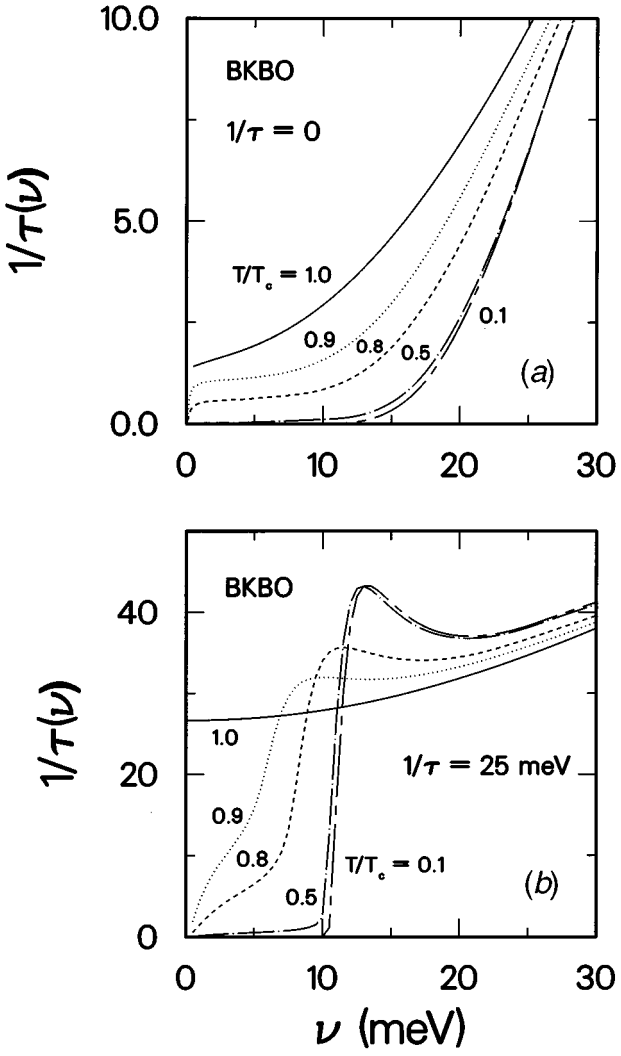

Fig. 23. Conductivity-derived scattering rate $1/\tau(\nu)$ versus frequency in the s-wave superconducting state for (a) $1/\tau = 0$ meV and (b) $1/\tau = 25$ meV, for temperatures as indicated. In both cases we used the BKBO spectrum with $\lambda = 1$. In (a) there is no signature for a gap, while one remains at low temperatures in (b).

It is clear from these results that there is a qualitative difference between the behaviour of superconductors with s- and d-wave order parameters. The low frequency behaviour of $1/\tau(\nu)$ thus provides information about the gap symmetry while the high frequency regime provides valuable information about the inelastic scattering processes and therefore possibly the pairing mechanism. In the case of YBCO the experiments definitely indicate very strong inelastic scattering with quasilinear frequency dependence, in agreement with the results presented here, based on a model spin fluctuation spectrum.

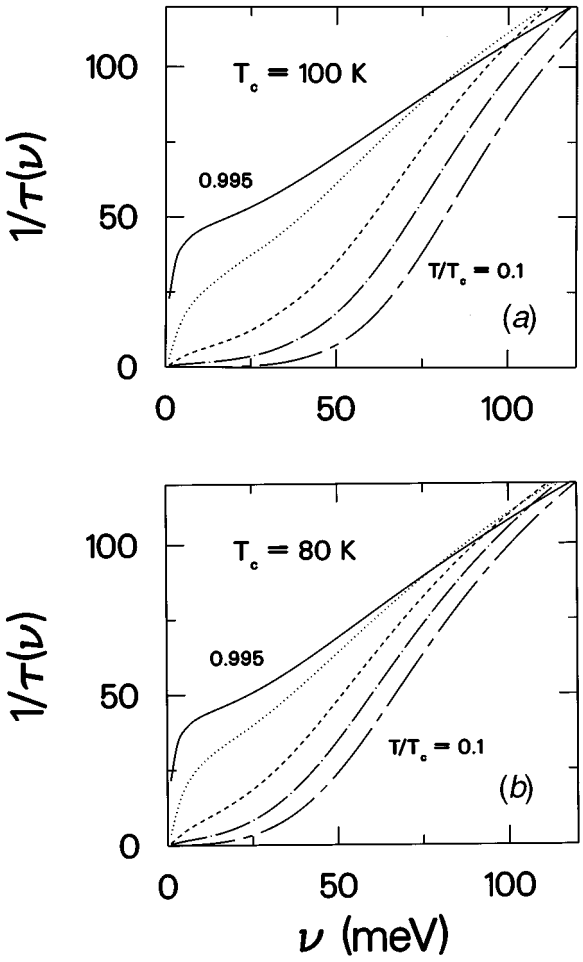

Fig. 24. Conductivity-derived scattering rate $1/\tau(\nu)$ versus frequency in the d-wave superconducting state for (a) $T_c = 100\,\mathrm{K}$ and (b) $T_c = 80\,\mathrm{K}$, reduced due to impurity scattering. In both cases we used the spin fluctuation spectrum appropriate to YBCO. In either case, as expected, there is no indication of a gap. The curve legend is the same as Figs 18 and 19.

5. Summary

We have discussed the optical conductivity in the far-infrared frequency range for both a normal metal and a superconductor. In either case we have included both elastic and inelastic scattering processes. In addition we have considered both an s-wave and a d-wave superconductor. We have adopted the standard assumptions for wide band metals, i.e. the validity of Migdal's theorem, the importance of Fermi surface interactions, and the neglect of vertex corrections in the optical conductivity. Some of our assumptions can easily be relaxed. For instance multiband models can be treated with special care devoted to the quasi-one-dimensional nature of chain-like bands, for example. The retention of vertex corrections is more difficult to implement; however, this approximation has been justified to some extent in past studies (Arnold and Swihart 1981;

Hirschfeld *et al.* 1993). It is also straightforward to include impurity scattering beyond the Born approximation (Hirschfeld *et al.* 1993, 1994).

In studying the optical properties of the high T_c oxide materials we have focussed on three quantities: the real and imaginary parts of the conductivity, and the scattering rate defined by equation (2). In the normal state the key signature of strong inelastic scattering has been identified as a strongly temperature-dependent and frequency-dependent scattering rate. These two independent variables play analogous roles, as can be appreciated by comparing the inverse lifetimes as a function of frequency, equations (35)–(37), to their counterparts as a function of temperature, equations (12)–(15). This means that either DC measurements as a function of temperature, or zero temperature measurements as a function of frequency, or some combination of these two can be carried out to probe the inelastic scattering processes.

In the superconducting state the signature of an s-wave gap is clearly evident in the real part of the conductivity, particularly when impurity scattering is present. The gap is more difficult to see in the clean limit, especially if there is no inelastic scattering. For a d-wave order parameter it is virtually impossible to see the gap develop in the superconducting state. Inelastic scattering does not alter these conclusions, but adds absorption at higher frequencies with structure which partially reflects the underlying boson spectrum.

The fact that the signature of an s-wave gap is present in the imaginary part of the conductivity is not widely recognised. For either strong elastic or inelastic scattering this signature tends to get smeared. Otherwise the imaginary part can be used as a gap probe as easily as the real part. In the case of a d-wave order parameter, the imaginary part is as poor at revealing the order parameter as the real part is. We have also extended the conductivity-derived scattering rate to the superconducting state. Its usefulness as a probe of scattering processes and gap values mimics that of the separate components of the conductivity just described. This scattering rate will be discussed in more detail in the following paper.

References

Allen, P. B., and Mitrović, B. (1982). *In* 'Solid State Physics', Vol. 37 (Eds H. Ehrenreich *et al.*), p. 1 (Academic: New York).
Arnold, G. B., and Swihart, J. C. (1981). *Sol. State Commun.* **37**, 303.
Ashcroft, N. W., and Mermin, N. D. (1976). 'Solid State Physics' (Holt, Rinehart and Winston: Philadelphia).
Atkinson, W. A., and Carbotte, J. P. (1995). *Phys. Rev.* B **52**, 10601.
Bardeen, J., Cooper, L. N., and Schrieffer, J. R. (1957). *Phys. Rev.* **108**, 1175.
Basov, D., Liang, R., Bonn, D. A., Hardy, W. N., Dabrowski, B., Quijada, M., Tanner, D. B., Rice, J. P., Ginsberg, D. M., and Timusk, T. (1995). *Phys. Rev. Lett.* **74**, 598.
Berlinsky, A. J., Kallin, C., Rose, G., and Shi, A.-C. (1993). *Phys. Rev.* B **48**, 4074.
Bickers, N. E., Scalapino, D. J., Collins, T., and Schlesinger, Z. (1990). *Phys. Rev.* B **42**, 67.
Carbotte, J. P., Jiang, C., Basov, D. N., and Timusk, T. (1995). *Phys. Rev.* B **51**, 11798.
Dolgov, O. V., Maksimov, E. G., and Shulga, S. V. (1991). *In* 'Electron–Phonon Interaction in Oxide Superconductors' (Ed. R. Baquero), p. 30 (World Scientific: Singapore).
Eliashberg, G. M. (1960). *Zh. Eksp. Teor. Fiz.* **38**, 966; *Sov. Phys. JETP* **11**, 696.
Farnworth, B., and Timusk, T. (1974). *Phys. Rev.* B **10**, 2799.
Grimvall, G. (1981). 'The Electron–Phonon Interaction in Metals' (North Holland: New York).
Hirschfeld, P. J., Puttika, W. O., and Scalapino, D. J. (1993). *Phys. Rev. Lett.* **71**, 3705.
Hirschfeld, P. J., Puttika, W. O., and Scalapino, D. J. (1994). *Phys. Rev.* B **50**, 10250.
Huang, Q., Zasadzinski, J. F., Tralshawala, N., Gray, K. E., Hinks, D. G., Tengand, J. L., and Greene, R. L. (1990). *Nature* **347**, 369.

Iye, Y. (1992). *In* 'Physical Properties of High T_c Superconductors III' (Ed. D. M. Ginsberg), p. 285 (World Scientific: Singapore).
Jiang, C., and Carbotte, J. P. (1996*a*). *Czech. J. Phys.* **46** (Suppl. S2), 973.
Jiang, C., and Carbotte, J. P. (1996*b*). *Phys. Rev.* B **53**, 11869.
Jiang, C., Schachinger, E., Carbotte, J. P., Basov, D., and Timusk, T. (1996). *Phys. Rev.* B **54**, 1264.
Joyce, R. R., and Richards, P. L. (1970). *Phys. Rev. Lett.* **24**, 1007.
Kamarás, K., Herr, S. L., Porter, C. D., Tache, N., Tanner, D. B., Etemad, S., Venkatesan, T., Chase, E., Inam, A., Wu, X. D., Hegde, M. S., and Dutta, B. (1990). *Phys. Rev. Lett.* **64**, 84.
Kubo, R. (1957). *J. Phys. Soc. Jpn* **12**, 570.
Lee, W., Rainer, D., and Zimmermann, W. (1989). *Physica* C **159**, 535.
Loong, C.-K., Vashishta, P., Kalia, R. K., Degani, M. H., Price, D. L., Jorgensen, J. D., Hinks, D. G., Dabrowski, B., Mitchell, A. W., Richards, D. R., and Zheng, Y. (1989). *Phys. Rev. Lett.* **62**, 2628.
Loong, C.-K., Hinks, D. G., Jin, W., Degani, M. H., Price, D. L., Jorgensen, J. D., Dabrowski, B., Mitchell, A. W., Richards, D. R., Zheng, Y., Vashishta, P., and Kalia, R. K. (1991). *In* 'Electron-Phonon Interaction in Oxide Superconductors' (Ed. R. Baquero), p. 122 (World Scientific: Singapore).
McMillan, W. L., and Rowell, J. M. (1969). *In* 'Superconductivity' (Ed. R. D. Parks), Vol. 1, p. 561 (Marcel Dekker: New York).
Mahan, G. D. (1981). 'Many-Particle Physics' (Plenum: New York).
Mahan, G. D. (1987). *Phys. Reports* **145**, 251.
Marsiglio, F., and Carbotte, J. P. (1995). *Phys. Rev.* B **52**, 16192.
Marsiglio, F., and Carbotte, J. P. (1997). *Aust. J. Phys.* **50**, 1011.
Marsiglio, F., Akis, R., and Carbotte, J. P. (1992). *Phys. Rev.* B **45**, 9865.
Marsiglio, F., Carbotte, J. P., Puchkov, A., and Timusk, T. (1996). *Phys. Rev.* B **53**, 9433.
Mattis, D. C., and Bardeen, J. (1958). *Phys. Rev.* **111**, 412.
Millis, A. J., Monien, H., and Pines, D. (1990). *Phys. Rev.* B **42**, 167.
Monthoux, P., and Pines, D. (1993). *Phys. Rev.* B **47**, 6069.
Nam, S. B. (1967). *Phys. Rev.* B **156**, 470; 487.
Nicol, E. J., Carbotte, J. P., and Timusk, T. (1991). *Phys. Rev.* B **43**, 473.
Puchkov, A. V., Timusk, T., Mosley, W. D., and Shelton, R. N. (1994). *Phys. Rev.* B **50**, 4144.
Puchkov, A. V., Timusk, T., Karlow, M. A., Cooper, S. L., Han, D. D., and Payne, D. A. (1996). *Phys. Rev.* B **54**, 6686.
Ron, A. (1963). *Phys. Rev.* **131**, 2041.
Scalapino, D. J. (1995). *Phys. Rep.* **250**, 329.
Schuttler, H. B., and Norman, M. R. (1996). *Phys. Rev.* B **54**, 13295.
Sharifi, F., Pargellis, A., Dynes, R. C., Miller, B., Hellman, E. S., Rosamilia, J., and Hartford, Jr., E. H. (1991). *Phys. Rev.* B **44**, 12521.
Shulga, S. V., Dolgov, O. V., and Maksimov, E. G. (1991). *Physica* C **178**, 266.
Tanner, D. B., and Timusk, T. (1992). *In* 'Physical Properties of High Temperature Superconductors III' (Ed. D. M. Ginsberg), p. 363 (World Scientific: Singapore).
Timusk, T., and Tanner, D. B. (1989). *In* 'Physical Properties of High Temperature Superconductors I' (Ed. D. M. Ginsberg), p. 339 (World Scientific: Singapore).
Varma, C. M., Littlewood, P. B., Schmitt-Rink, S., Abrahams, E., and Ruckenstein, A. (1989). *Phys. Rev. Lett.* **64**, 497 (E).
Varma, C. M., Littlewood, P. B., Schmitt-Rink, S., Abrahams, E., and Ruckenstein, A. (1990). *Phys. Rev. Lett.* **63**, 1996.
Zasadzinski, J. F., Tralshawala, N., Huang, Q., Gray, K. E., and Hinks, D. G. (1991). *In* 'Electron–Phonon Interaction in Oxide Superconductors' (Ed. R. Baquero), p. 46 (World Scientific: Singapore).
Zhou, C., and Schulz, H. J. (1992). *Phys. Rev.* B **45**, 7397.
Ziman, J. M. (1972). 'Principles of the Theory of Solids' (Cambridge Univ. Press).
Zimmerman, W., Brandt, E. H., Bauer, M., Seider, E., and Genzel, L. (1991). *Physica* C **183**, 99.

Manuscript received 17 January, accepted 15 July 1997